

Multimodel assessment of the upper troposphere and lower stratosphere: Extratropics

M. I. Hegglin,¹ A. Gettelman,² P. Hoor,³ R. Krichevsky,¹ G. L. Manney,^{4,5} L. L. Pan,² S.-W. Son,⁶ G. Stiller,⁷ S. Tilmes,² K. A. Walker,^{1,8} V. Eyring,⁹ T. G. Shepherd,¹ D. Waugh,¹⁰ H. Akiyoshi,¹¹ J. A. Añel,¹² J. Austin,¹³ A. Baumgaertner,³ S. Bekki,¹⁴ P. Braesicke,¹⁵ C. Brühl,³ N. Butchart,¹⁶ M. Chipperfield,¹⁷ M. Dameris,⁹ S. Dhomse,¹⁷ S. Frith,¹⁸ H. Garny,⁹ S. C. Hardiman,¹⁶ P. Jöckel,^{3,9} D. E. Kinnison,² J. F. Lamarque,² E. Mancini,¹⁹ M. Michou,²⁰ O. Morgenstern,^{15,21} T. Nakamura,¹¹ D. Olivié,²⁰ S. Pawson,¹⁸ G. Pitari,¹⁹ D. A. Plummer,²² J. A. Pyle,¹⁵ E. Rozanov,^{23,24} J. F. Scinocca,²⁵ K. Shibata,²⁶ D. Smale,²¹ H. Teyssède,²⁰ W. Tian,¹⁷ and Y. Yamashita¹¹

Received 17 January 2010; revised 7 June 2010; accepted 21 June 2010; published 23 October 2010.

[1] A multimodel assessment of the performance of chemistry-climate models (CCMs) in the extratropical upper troposphere/lower stratosphere (UTLS) is conducted for the first time. Process-oriented diagnostics are used to validate dynamical and transport characteristics of 18 CCMs using meteorological analyses and aircraft and satellite observations. The main dynamical and chemical climatological characteristics of the extratropical UTLS are generally well represented by the models, despite the limited horizontal and vertical resolution. The seasonal cycle of lowermost stratospheric mass is realistic, however with a wide spread in its mean value. A tropopause inversion layer is present in most models, although the maximum in static stability is located too high above the tropopause and is somewhat too weak, as expected from limited model resolution. Similar comments apply to the extratropical tropopause transition layer. The seasonality in lower stratospheric chemical tracers is consistent with the seasonality in the Brewer-Dobson circulation. Both vertical and meridional tracer gradients are of similar strength to those found in observations. Models that perform less well tend to use a semi-Lagrangian transport scheme and/or have a very low resolution. Two models, and the multimodel mean, score consistently well on all diagnostics, while seven other models score well on all diagnostics except the seasonal cycle of water vapor. Only four of the models are consistently below average. The lack of tropospheric chemistry in most models limits their evaluation in the upper troposphere. Finally, the UTLS is relatively sparsely sampled by observations, limiting our ability to quantitatively evaluate many aspects of model performance.

¹Department of Physics, University of Toronto, Toronto, Ontario, Canada.

²Atmospheric Chemistry Division, National Center for Atmospheric Research, Boulder, Colorado, USA.

³Max Planck Institut für Chemie, Mainz, Germany.

⁴Jet Propulsion Laboratory, California Institute of Technology, Pasadena, California, USA.

⁵New Mexico Institute of Mining and Technology, Socorro, New Mexico, USA.

⁶Department of Atmospheric and Oceanic Sciences, McGill University, Montreal, Quebec, Canada.

⁷Karlsruhe Institute of Technology, Institute for Meteorology and Climate Research, Karlsruhe, Germany.

⁸Department of Chemistry, University of Waterloo, Waterloo, Canada.

⁹Deutsches Zentrum für Luft- und Raumfahrt, Institut für Physik der Atmosphäre, Oberpfaffenhofen, Germany.

¹⁰Johns Hopkins University, Baltimore, Maryland, USA.

¹¹National Institute for Environmental Studies, Tsukuba, Japan.

¹²Environmental Physics Laboratory, Universidade de Vigo, Ourense, Spain.

¹³Geophysical Fluid Dynamics Laboratory, NOAA, Princeton, New Jersey, USA.

¹⁴LATMOS, Institut Pierre-Simone Laplace, UVSQ, UMPC, CNRS/INSU, Paris, France.

¹⁵Department of Chemistry, Cambridge University, UK.

¹⁶Met Office, Exeter, UK.

¹⁷School of Earth and Environment, University of Leeds, Leeds, UK.

¹⁸Global Modelling and Assimilation Office, NASA Goddard Space Flight Center, Greenbelt, Maryland, USA.

¹⁹Dipartimento di Fisica, Università degli Studi di L'Aquila, L'Aquila, Italy.

²⁰GAME/CNRM, Météo-France, CNRS, Toulouse, France.

²¹National Institute of Water and Atmospheric Research, Lauder, New Zealand.

²²Environment Canada, Toronto, Ontario, Canada.

²³Physikalisch-Meteorologisches Observatorium Davos, Davos, Switzerland.

²⁴Institute for Atmospheric and Climate Science, ETH, Zurich, Switzerland.

²⁵Canadian Centre for Climate Modelling and Analysis, Victoria, British Columbia, Canada.

²⁶Meteorological Research Institute, Tsukuba, Japan.

Citation: Hegglin, M. I., et al. (2010), Multimodel assessment of the upper troposphere and lower stratosphere: Extratropics, *J. Geophys. Res.*, 115, D00M09, doi:10.1029/2010JD013884.

1. Introduction

[2] The upper troposphere/lower stratosphere (UTLS) plays an important role in the radiative forcing of the climate system and in chemistry-climate coupling [Shepherd, 2007]. Changes in the extratropical UTLS determine the stratospheric influence on the troposphere through for example the transport of stratospheric ozone into the troposphere, UV fluxes [Hegglin and Shepherd, 2009], or radiative forcing of the surface climate [Solomon et al., 2010]. It is therefore important that chemistry-climate models (CCMs) used for the prediction of the ozone layer and climate change represent accurately the chemical and dynamical structures of the UTLS. For the first time, a multimodel assessment with focus on the extratropical UTLS has been performed within phase 2 of the Chemistry-Climate Model Validation activity (CCMVal-2) of the World Climate Research Programme's Stratospheric Processes and their Role in Climate (SPARC) project. The tropical UTLS and global UTLS trends have been assessed in a companion paper by Gettelman et al. [2010].

[3] The focus of the multimodel assessment presented here is the extratropical UTLS, which is here defined as the region between the mid-troposphere (approx. 5 km) and the upper boundary of the tropically controlled transition region (around 22 km [Rosenlof et al., 1997]). It includes the lowermost stratosphere (LMS), the region between the extratropical tropopause and the 380 K potential temperature surface [Holton et al., 1995], which is equivalent to the stratospheric part of the 'middleworld' [Hoskins, 1991]. Chemical trace gas distributions in the extratropical UTLS are shaped by the tropopause and determined by transport processes on various time and length scales. The effect of transport is greatest on the shorter-lived greenhouse gases water vapor and ozone (with lifetimes of up to one year), and much less on the longer-lived, well-mixed greenhouse gases such as CH₄ or CFCs (with lifetimes of several decades). Thus, it is most critical to characterize the distributions of ozone and water vapor. A defining characteristic of the LMS is that isentropes intersect the tropopause, thereby potentially connecting the troposphere and the stratosphere via rapid quasi-adiabatic motion. The slower diabatic circulation in the stratosphere (the Brewer-Dobson circulation) is predominantly downward in the extratropics, which on its own would transport aged stratospheric air into the LMS. However, meridional mixing from the tropical UTLS transports younger air masses to mid and high latitudes and 'rejuvenates' air as it slowly descends into the LMS [Rosenlof et al., 1997; Bregman et al., 2000; Hegglin and Shepherd, 2007], an effect quantified by Hoor et al. [2005] and Bönisch et al. [2009]. The lower boundary of the LMS is defined by the tropopause, which is here defined by a dynamical quantity. Distributions of chemical tracers that are affected by transport exhibit strong spatial gradients across the tropopause in a layer of finite depth referred to as the extratropical tropopause transition layer

(ExTL) [Fischer et al., 2000; Zahn et al., 2000; Hoor et al., 2002]. The ExTL is a global feature with increasing depth towards high latitudes, and has been found to be different for different tracers [Hegglin et al., 2009]. The transition has been interpreted as the result of recurrent wave-breaking events, forced by synoptic-scale baroclinic disturbances, which stir tropospheric and stratospheric air masses with very different chemical and radiative characteristics [Shepherd, 2007]. Indeed, Berthet et al. [2007] have shown that stratosphere-troposphere exchange events traced by Lagrangian backward trajectories calculated from large-scale wind fields of the ECMWF reanalyses reveal the layer of tropospheric influence just above the tropopause. Small-scale processes such as three-dimensional turbulence and ultimately molecular diffusion then act to reduce these inhomogeneities.

[4] The radiative properties of the UTLS are determined by the distributions of greenhouse gases, aerosols, and clouds. The low temperatures in this region lead to a net radiative cooling that is close to zero around the tropopause, which implies a strong temperature sensitivity to radiative changes [Clough and Iacono, 1995]. Moreover the large contrast between the low temperatures around the tropopause and the higher temperatures at the surface means that changes in the radiative properties of the tropopause region make a particularly strong contribution to the greenhouse effect. This sensitivity has been quantified by Forster and Shine [1997], who found that the Earth's surface temperature response to an ozone perturbation is maximized when the perturbation is introduced around the tropopause.

[5] The dynamical properties of the UTLS are directly dependent on the radiative properties of this region since the prevailing latitudinal temperature gradients affect the strength and location of the subtropical jet, which organizes eddy fluxes and surface pressure distributions [Randel and Held, 1991]. These eddy fluxes appear to play a key role in stratosphere-troposphere coupling [Baldwin and Dunkerton, 2001; Thompson et al., 2006], and suggest a way in which stratospheric processes may affect tropospheric weather and regional climate [e.g., Thompson and Wallace, 1998].

[6] Chemical, radiative, and dynamical processes are all important for maintaining the structure in chemical tracer distributions and physical quantities in the UTLS. These structures can therefore be used to validate indirectly the CCMs' representation of these processes. In this multimodel evaluation, we focus in a first step on how well the CCMs represent the main dynamical and chemical climatological structures of the UTLS. The evaluation is only capable of revealing the weaknesses or strengths of the models; it does not give us the reasons why a model performs well or badly, since these reasons are invariably model-specific. In Section 2 we introduce the participating models and the observations used for the comparisons. Section 3 describes the different diagnostics and metrics used to qualitatively and quantitatively gauge the models' performance in reproducing key features observed in the extratropical UTLS. The results are shown in Section 4, before we come

Table 1. Number, Name, Key References, Transport Scheme, Horizontal Resolution, and Number of Vertical Levels in the UTLS Between 300 and 100 hPa of Participating CCMs

Number	CCM	Reference	Transport Scheme ^a	Horizontal Resolution	Levels in UTLS
1	AMTRAC3	<i>Austin and Wilson</i> [2010]	FV	≈200 km	7
2	CAM3.5	<i>Lamarque et al.</i> [2008]	FV	1.9° × 2.5°	7
3	CCSRNIES	<i>Akiyoshi et al.</i> [2009]	STFD	T42	6
4	CMAM	<i>Scinocca et al.</i> [2008] <i>de Grandpré et al.</i> [2000]	Spectral	T31	7
5	CNRM-ACM	<i>Déqué</i> [2007]	SL cubic	T42	8
6	E39CA	<i>Teyssédre et al.</i> [2007] <i>Stenke et al.</i> [2009] <i>Garny et al.</i> [2009]	ATTILA	T30	15
7	EMAC	<i>Jöckel et al.</i> [2006]	FFSL	T42	12
8	GEOSCCM	<i>Pawson et al.</i> [2008]	FV	2° × 3.75°	7
9	LMDZrepro	<i>Jourdain et al.</i> [2008]	FV	2.5° × 2.5°	8
10	MRI	<i>Shibata and Deushi</i> [2008a, 2008b]	FFSL	T42	6
11	Niwa-SOCOL	<i>Schraner et al.</i> [2008] <i>Egorova et al.</i> [2005]	Hybrid	T30	5
12	SOCOL	<i>Schraner et al.</i> [2008] <i>Egorova et al.</i> [2005]	Hybrid	T30	5
13	ULAQ	<i>Pitari et al.</i> [2002] <i>Eyring et al.</i> [2006, 2007]	FFEE	11.5° × 22.5°	3
14	UMETRAC	<i>Austin and Butchart</i> [2003]	FV	2.5° × 3.75°	9
15	UMSLIMCAT	<i>Tian and Chipperfield</i> [2005] <i>Tian et al.</i> [2006]	FV	2.5° × 3.75°	9
16	UMUKCA-METO	<i>Morgenstern et al.</i> [2009]	SL, quasi-cubic	2.5° × 3.75°	7
17	UMUKCA-UCAM	<i>Morgenstern et al.</i> [2009]	SL, quasi-cubic	2.5° × 3.75°	7
18	WACCM	<i>Garcia et al.</i> [2007]	FV	1.9° × 2.5°	7

^aTransport scheme abbreviations: FV, finite volume; FFSL, flux-form semi-Lagrangian; SL, semi-Lagrangian; STFD, spectral transform and finite difference; FFEE, flux form Eulerian explicit; ATTILA, fully Lagrangian.

to the discussion of the performance of each model in Section 5, and a summary and recommendations in Section 6.

2. Models and Observations

2.1. Models

[7] Eighteen chemistry-climate models (CCMs; see Table 1) are evaluated in this multimodel assessment focusing on the extratropical UTLS. All the CCMs used here participated in the CCMVal-2 intercomparison [Eyring et al., 2008]. The CCMs are fully interactive models with a comprehensive stratosphere which aim to represent the coupling between chemistry and climate in order to simulate and predict the evolution of the stratospheric ozone layer over the past 50 years and the 21st century. For this purpose different past and future long-term simulations have been run using specified greenhouse gas and halogen scenarios. Details on the model specifications and the simulations are given by Morgenstern et al. [2010]. Note that CMAM is the only model coupled to a dynamical ocean. For the diagnostics presented in this study, we used model data obtained from past simulations extending from 1960 to 2007 and using observed SSTs (REF-B1; see Morgenstern et al. [2010] for a detailed explanation of the simulation setup).

2.2. Observations

[8] Observations of chemical species in the UTLS are still relatively sparse considering the large temporal and spatial variations and gradients in tracer concentrations in this region. In-situ observations are difficult to obtain due to the

low pressures and temperatures. Satellite measurements in the upper troposphere are often obscured by clouds, and are moreover subject to significant spatial smearing. For this reason, different observations had to be compiled and validated prior to their use in this multimodel validation effort.

2.2.1. Aircraft Data

[9] Aircraft observations are generally characterized by high accuracy, high precision, and high resolution data in the UTLS, but are restricted in their representativeness due to limited sampling in time and space.

[10] Data from various NASA, NOAA and German aircraft campaigns between 1995 and 2008 have recently been compiled into a high resolution aircraft based UTLS climatology of ozone, CO and H₂O [Tilmes et al., 2010]. The data set covers a broad altitude range up to 22 km. The spatial coverage ranges over all latitudes in the NH for most of the four seasons, but coverage is predominantly over North America and Europe. The precision and accuracy of the ozone data are ±5%. CO observations taken by different instruments have a precision of <1% and an accuracy of <3%. The precision of H₂O data is estimated to be <5% and the accuracy is between 0.3 ppmv and values of 10% depending on the instrument. A key purpose of the aircraft climatology is to serve as a tool to evaluate the representation of chemistry and transport by CCMs in the UTLS.

[11] A subset of those high-resolution and high-precision observations used in this paper separately has been provided by the German SPURT (Trace Gas Transport in the Tropopause Region) aircraft campaign [Engel et al., 2006]. The campaign consisted of 8 deployments distributed seasonally

over the course of three years (2001–2003), with a total of 36 flights, each yielding around 2–5 hours of observations. The flights were carried out between around 35°N and 75°N over Europe and reached potential temperature levels between 370 K and 375 K. CO typically showed a total uncertainty of 1.5% [Hoor *et al.*, 2004].

[12] The other subset of high-resolution data is from the NASA POLARIS (Photochemistry of Ozone Loss in the Arctic Region in Summer) campaign [Newman *et al.*, 1999]. During the campaign, 35 flights using the NASA ER-2 research aircraft were deployed from three locations at mid- to high-latitudes with flights covering latitudes between $\approx 20^\circ\text{N}$ and 70°N , a vertical range of 5 to 18 km, and March to September 1997. A large suite of in-situ measurements was made on board the ER-2. For the O₃ and H₂O data used in this study, the estimated accuracies are $\approx 3\%$ and 5% , respectively [Hintsa *et al.*, 1999]. The use of these data to characterize the ExTL has been described by Pan *et al.* [2004, 2007].

2.2.2. Satellite Data

[13] Satellite instruments have recently achieved the technological maturity to measure the UTLS from space, offering unprecedented temporal and spatial coverage of this region. Investigating the accuracy and precision of these measurements is the focus of intensive validation efforts. We describe here the data from four different satellite instruments used in this paper.

2.2.2.1. ACE-FTS on SCISAT-1

[14] The Atmospheric Chemistry Experiment Fourier Transform Spectrometer (ACE-FTS) on Canada's SCISAT-1 satellite features high resolution (0.02 cm^{-1}) and broad spectral coverage in the infrared (750 to 4400 cm^{-1}) [Boone *et al.*, 2005; Bernath *et al.*, 2005]. The instrument has operated since February 2004 in solar occultation mode providing seasonally varying coverage of the globe, with an emphasis on mid-latitudes and the polar regions. Up to 30 occultation events occur per calendar day. The very high signal-to-noise ratio characterizing the ACE-FTS infrared spectra makes it possible to measure more than 30 chemical trace gas species with high accuracy and precision throughout the stratosphere and lower mesosphere [Clerbaux *et al.*, 2008; Dupuy *et al.*, 2009], and also in the UTLS [Hegglin *et al.*, 2008]. This, together with vertical sampling ranging from about 3 km to less than 1 km in the UTLS, provides the first global view of tracer distributions in the extratropical tropopause region [Hegglin *et al.*, 2009].

2.2.2.2. Aura MLS

[15] The Microwave Limb Sounder (MLS) on the EOS Aura satellite measures millimeter- and submillimeter-wavelength thermal emission from the limb of Earth's atmosphere [Waters *et al.*, 2006]. Aura MLS has data coverage from 82°S to 82°N latitude on every orbit, providing comprehensive information on UTLS tracer distributions. Vertical profiles are measured every 165 km along the suborbital track and have a horizontal resolution of ≈ 200 – 300 km along-track and ≈ 3 – 9 km across-track. Vertical resolution of the Aura MLS data is typically ≈ 3 – 4 km in the lower and middle stratosphere [Livesey *et al.*, 2007]. O₃ has been used successfully in studies to examine transport in the UTLS, although some biases still exist in the version 2.2 which is used in the evaluations presented here. Validation of UTLS O₃ is discussed by Livesey *et al.* [2008].

2.2.2.3. MIPAS

[16] MIPAS is a limb-viewing Fourier transform emission spectrometer covering the mid-infrared spectral region between 685 and 2410 cm^{-1} [Fischer *et al.*, 2008] on board Envisat in a sun-synchronous polar orbit. MIPAS has provided data since 2002 at about 1000 geo-locations per day from pole to pole during day and night. It covers the atmosphere from the upper troposphere to the mesosphere (6 to 70 km), thus MIPAS provides global distributions of a large number of species. In its original observation set-up from July 2002 to March 2004 it measured one limb radiance profile every 500 km along track with a vertical sampling of 3 km and a spectral resolution of 0.035 cm^{-1} . Validation of these data products is provided by Milz *et al.* [2005, 2009], Wang *et al.* [2007], and Steck *et al.* [2007]. Since January 2005, the observation set-up has been changed to slightly reduced spectral resolution (0.0625 cm^{-1}), but improved vertical (1.5 km) and horizontal along-track (400 km) sampling. Description of these data products is given by von Clarmann *et al.* [2009]. In this study we use MIPAS O₃, H₂O, and HNO₃ observations which have been processed at the Institute for Meteorology and Climate Research (IMK) [von Clarmann *et al.*, 2003].

2.2.2.4. Global Positioning System Radio Occultation Data

[17] The Global Positioning System Radio Occultation (GPS RO) data used in this study were obtained from the COSMIC/FORMOSAT-3 (Formosa Satellite Mission 3) mission, which is a collaborative project between Taiwan and the United States [Anthes *et al.*, 2008]. The mission placed six micro-satellites in different orbits at 700–800 km above the ground. These satellites form a low-orbit constellation that receives signals from US GPS satellites, providing approximately 2500–3000 soundings per day almost evenly distributed over the globe. The mission has a relatively short data record since its mission launch was only in 2006. In this study, we use GPS RO retrieved temperature data between 2006 and 2009.

2.2.3. Meteorological Reanalyses

[18] For the comparisons of dynamical fields we use meteorological reanalyses such as the ERA-40 data set from the European Centre for Medium Range Weather Forecasts (ECMWF) and NCEP from the National Centers for Environmental Prediction and National Center for Atmospheric Research. ERA-40 and NCEP both have a horizontal resolution of $2.5^\circ \times 2.5^\circ$, and exhibit 8 and 6 vertical layers in the UTLS between 300 and 100 hPa, respectively. For a more detailed description of these data sets we refer to Uppala *et al.* [2005], Kalnay *et al.* [1996], Randel *et al.* [2003], and SPARC [2002].

3. Diagnostics and Performance Metrics

[19] Diagnostics and performance metrics are used to evaluate model performance in the UTLS in a qualitative and quantitative way, respectively.

3.1. Diagnostics

[20] The diagnostics are chosen to evaluate the main characteristics of dynamics and transport in the UTLS in the models. The main characteristics include the seasonality in the background LMS tracer distributions and LMS mass

Table 2. Diagnostics Used for the Multimodel Assessment^a

Process	Diagnostic	Variables	Observations	Reference ^b
Dynamics	Zonal mean zonal wind @200 hPa ^c	U (Zonal Wind)	ERA-40, NCEP	
	Seasonal cycle in LMS mass ^c	M (Mass)	ERA-40	<i>Appenzeller et al.</i> [1996]
	TP pressure anomalies	P (Pressure)	ERA-40, NCEP	
	TP inversion layer	T (Temperature)	GPS	<i>Birner et al.</i> [2002], <i>Birner</i> [2006] <i>Randel et al.</i> [2007] <i>Logan et al.</i> [1999]
Transport and mixing	Seasonal cycle of tracers @100 and 200 hPa ^c	O ₃ , HNO ₃ , H ₂ O	MIPAS, MLS ACE-FTS	<i>Shepherd</i> [2002]
	Meridional tracer gradients @200 hPa ^c	O ₃	MLS	
	Normalized CO relative to TP ^c	CO	SPURT	<i>Hoor et al.</i> [2004, 2005]
	Vertical profiles in TP coordinates ^c	H ₂ O and CO	Aircraft, ACE-FTS	<i>Pan et al.</i> [2004, 2007]; <i>Hegglin et al.</i> [2009]
	ExTL depth from tracer-tracer correlations	H ₂ O/O ₃	Aircraft	<i>Pan et al.</i> [2007]; <i>Hegglin et al.</i> [2009]

^aTP denotes tropopause.^bAdditional literature with information on the data sets or the diagnostics.^cDiagnostics which are used for final grading of the CCMs.

determined by the seasonally varying strength of the Brewer-Dobson circulation, as well as the fine-scale structure of the transition between the troposphere and the stratosphere determined by synoptic and smaller scale eddies. Both these classes of characteristics are important for determining surface climate and stratosphere-troposphere coupling, and can be tested with different diagnostics. The full list of diagnostics used for the validation of the CCMVal-2 models in the extratropical UTLS is given in Table 2. The following sections provide in addition short descriptions of each diagnostic:

3.1.1. Diagnostic 1

[21] The seasonal zonal mean zonal wind is used to test the models' realism in representing the meridional gradients of the thermal structure.

3.1.2. Diagnostic 2

[22] The seasonal cycle of LMS mass [*Appenzeller et al.*, 1996] is a basic test of the response of the atmosphere to a combination of direct radiative forcing through changes in UTLS temperatures as well as of dynamical forcing through the wave-driven Brewer-Dobson circulation. It can be seen as a basic measure of the vertical structure in a model.

3.1.3. Diagnostic 3

[23] Interannual anomalies in extratropical tropopause pressure are used as a measure of the response of the models to different forcings such as volcanoes, ENSO, etc. They are strongly related to the LMS mass.

3.1.4. Diagnostic 4

[24] The tropopause inversion layer (TIL) [*Birner et al.*, 2002; *Birner*, 2006] is a distinctive feature of the thermal structure of the tropopause, which reflects the balance between radiative and dynamical processes. The formation of the TIL has been interpreted as a result of large-scale dynamics or convection, but also seems to be forced or maintained through the distributions of the radiatively active species O₃ and H₂O. This diagnostic extends diagnostic 6 from *Gottelman et al.* [2010] to the extratropics.

3.1.5. Diagnostic 5

[25] The seasonal cycles of O₃, HNO₃, and H₂O at 100 and 200 hPa are used to test the models' representation of the seasonally varying strength in large-scale transport through the diabatic Brewer-Dobson circulation, and in quasi-horizontal transport (and subsequent mixing) between the tropics and the extratropics within the tropically controlled transition region (380–420 K, or ≈100 hPa) or across the subtropical jet (340–380 K, or ≈200 hPa).

3.1.6. Diagnostic 6

[26] The meridional gradient of O₃ is a measure of the chemical distinctiveness (i.e., different air masses can be readily distinguished by their chemical composition) of the UTLS in latitude, and therefore of the degree of isolation of different regions such as the tropics and the extratropics.

3.1.7. Diagnostic 7

[27] Vertical profiles of normalized CO in tropopause coordinates (here potential temperature units relative to the potential temperature at the 2 PVU tropopause) allow us to separate transport into the LMS across the extratropical tropopause on short time scales from transport from the tropical and subtropical UT on longer time scales. It thereby helps to determine the tropospheric influence on the lowermost stratospheric background. The CO is normalized with respect to the mean tropospheric value, in order to remove discrepancies between model and measurements arising from the different tropospheric boundary specification of CO used in the models.

3.1.8. Diagnostic 8

[28] Mean annual profiles of H₂O and CO in tropopause coordinates (here kilometers relative to the thermal tropopause height) at mid-latitudes and northern hemisphere polar regions provide a critical diagnostic for testing the degree of vertical distinctiveness of the UT and LS, as well as to obtain information on chemical processes that determine the tracer profiles.

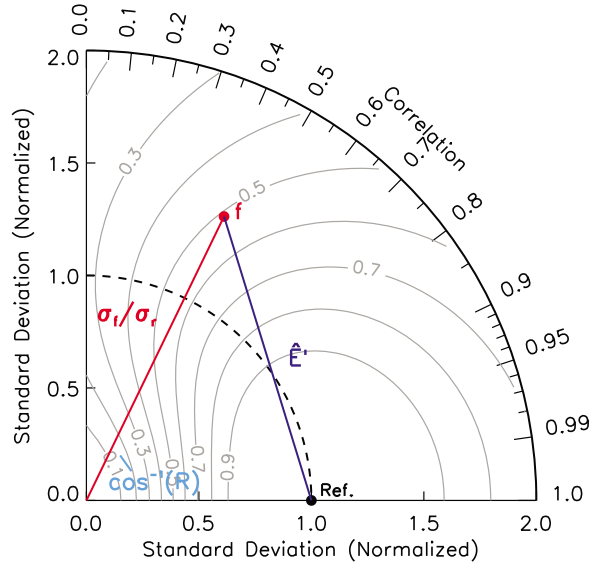


Figure 1. Taylor diagram describing the pattern statistics between a test (f) and a reference field (r , here denoted with $Ref.$). The inverse cosine of the correlation R (indicated in light blue) determines the location on the azimuthal axis. The radial distance of f from the origin corresponds to the standard deviation of the test field normalized by the standard deviation of the reference field (σ_f/σ_r , red line). The normalized pattern RMS difference (E' , dark blue line) between test and reference field corresponds to the distance between the two fields on the diagram. Gray thin lines indicate the skill score (S) of the test field, here a value of 0.51.

3.1.9. Diagnostic 9

[29] The depth of the extratropical tropopause transition layer (ExTL) based on the tracer-tracer correlation method using H_2O-O_3 by *Pan et al.* [2007] and its location relative to the thermal tropopause are used to diagnose the mixing and transport characteristics of the models in the tropopause region.

3.2. Performance Metrics and Grading

[30] Performance metrics provide statistical measures of agreement between the model field and observational data sets. The following metrics are used in this study to quantitatively assess the ability of the CCMs to reproduce patterns and mean state of the extratropical UTLS. While errors in the mean are simply defined (see Section 3.2.2), errors in the patterns are more complicated since they can arise as a result of errors in either phase or amplitude. How can we visualize this information in a simple way?

3.2.1. Taylor Diagrams

[31] An answer to the above question is provided by Taylor diagrams (*Taylor* [2001] and Figure 1). Taylor diagrams provide a statistical summary of how well two patterns from a test (i.e. the model) field (f) and a reference (i.e. the observational) field (r) of the same quantity match each other in terms of their correlation (R), their pattern root-mean-square (RMS) difference (E'), and the ratio of their standard deviations (σ_f/σ_r). Taylor diagrams have been widely used to test various aspects of model performance, as for example in the IPCC TAR [*Intergovernmental Panel on*

Climate Change, 2001] or in chemistry transport model inter-comparisons [*Brunner et al.*, 2003, 2005]. The Pearson's correlation R used here as the first metric is given by

$$R = \frac{\frac{1}{N} \sum_{n=1}^N (f_n - \bar{f})(r_n - \bar{r})}{\sigma_f \sigma_r} \quad (1)$$

For seasonal cycles n denotes the month of the year and N is 12, while for latitudinal structure n indexes the latitude and N is the total number of latitude bins. For the calculation of the spatial correlation, the model data need to be interpolated onto the latitude of the observations. In statistics the quantification of the difference between the two fields r and f is most often given by the root-mean-square (RMS) difference

$$E = \sqrt{\left[\frac{1}{N} \sum_{n=1}^N (f_n - r_n)^2 \right]} \quad (2)$$

and the full-mean square difference between f and r by

$$E^2 = \bar{E}^2 + E'^2 \quad (3)$$

where

$$\bar{E} = \bar{f} - \bar{r} \quad (4)$$

is the mean bias and

$$E' = \sqrt{\frac{1}{N} \sum_{n=1}^N [(f_n - \bar{f}) - (r_n - \bar{r})]^2} \quad (5)$$

quantifies the magnitude of the mismatch between the two patterns (the pattern RMS difference). Normalizing E' by σ_r , i.e., $\hat{E}' = E'/\sigma_r$, it is easily shown that

$$\hat{E}'^2 = (\sigma_f^2 + \sigma_r^2 - 2\sigma_f\sigma_r R) / \sigma_r^2 = \frac{\sigma_f^2}{\sigma_r^2} + 1 - 2\frac{\sigma_f}{\sigma_r} R \quad (6)$$

so that \hat{E}' is determined once σ_f/σ_r and R are known. Smaller \hat{E}' (i.e. the closer f and r are to each other) represent a better fit between the test field and the reference field. The Taylor diagram uses σ_f/σ_r and R as radial and azimuthal coordinates, respectively. By scaling R by its inverse cosine, it turns out that \hat{E}' exactly corresponds to the distance in the diagram from the reference point [*Taylor*, 2001].

[32] An illustrative example of a Taylor diagram is provided in Figure 2. Different test fields ($T1$, $T2$, .. $T5$, in color) are depicted together with a reference field (in black) in Figure 2 (left). The pattern statistics between the test and the reference field are then transferred into the Taylor diagram on the right. $T1$ has the exact phase and amplitude as the reference field, and therefore lies on top of the reference field in the Taylor diagram, despite the fact that the test field is offset by 2 units in the y-direction. Taylor diagrams do not provide information on the mean error, and we need therefore to have an additional grading of the mean to get full information on the model performance (see Section 3.3.2). $T2$ and $T3$ have the exact phase (and therefore maximal correlation R), but different amplitudes which correspond to normalized standard deviations greater and less than unity,

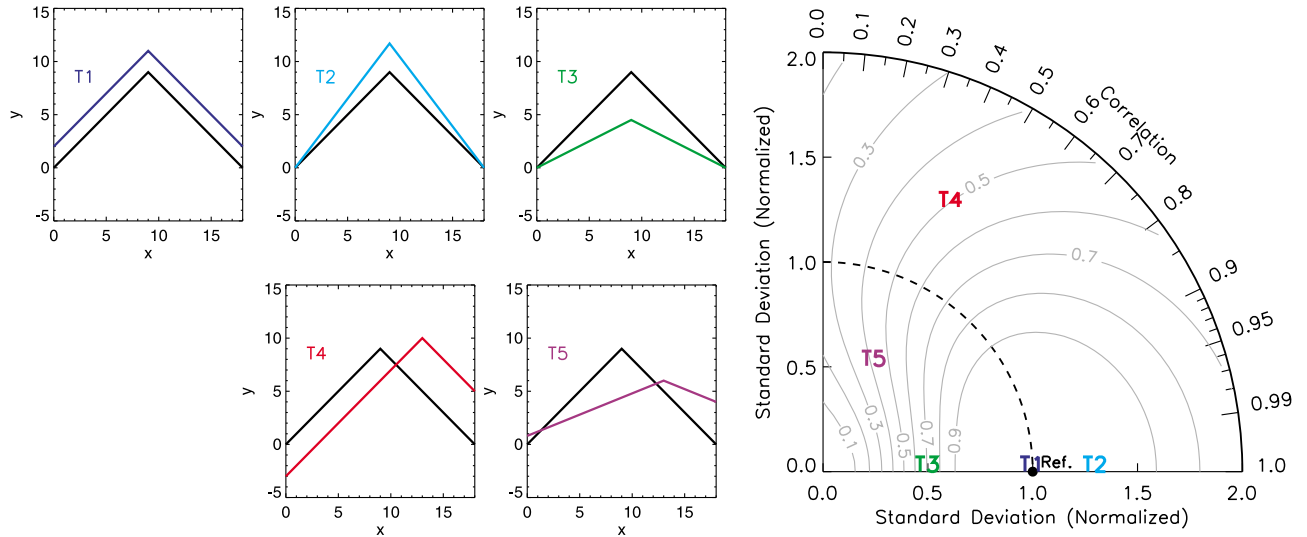


Figure 2. Illustrated are (left) examples of test (color coded) and reference fields (in black) and (right) their pattern statistics in the Taylor diagram. See text for explanation.

moving them further away and closer to the origin, respectively. It follows that \hat{E}' increases. $T4$ and $T5$ have both different phases and different amplitudes, which decreases the correlation R and increases \hat{E}' even further.

[33] From Figures 1 and 2 it is clear that a certain value of \hat{E}' can be obtained by different combinations of R and σ_f/σ_r . How do we gauge the relative skills of two models that obtain the same \hat{E}' but where one has a better phase and the other a better amplitude? For this purpose, we can define a skill score (S) following Taylor [2001] which ensures that at a fixed phase or amplitude the skill increases monotonically with improvements in amplitude or phase, respectively, and with values between 0 and 1:

$$S = \frac{4(1 + R)}{(\hat{\sigma} + 1/\hat{\sigma})^2(1 + R_0)} \quad (7)$$

Here, $\hat{\sigma}$ (σ_f/σ_r) denotes the standard deviation of the test field normalized by the standard deviation of the reference field, and R_0 is the maximum correlation that models can achieve. Choosing $R_0 < 1$ allows us to account for uncertainty in the observations or model limitations such as spatial and temporal resolution. The skill (S) approaches unity as the model variance approaches the observed variance (i.e., as $\hat{\sigma} \rightarrow 1$) and as $R \rightarrow R_0$. The skill score is indicated with gray lines in Figures 1 and 2.

3.2.2. Climatological Mean State Metrics

[34] As mentioned in the previous section, Taylor diagrams do not yield information on how close the mean of a given test field is to that of the reference field. We therefore use in addition to the skill factor as defined in equation (7), a grading for the mean values as introduced by Douglass *et al.* [1999], which also has been applied within CCMVal-1 [Waugh and Eyring, 2008] and by Gettelman *et al.* [2010]:

$$g_m = \max\left(0, 1 - \frac{1}{N} \sum_{i=1}^N \frac{|\mu_{i,obs} - \mu_{i,mod}|}{n_g \sigma_{i,obs}}\right) \quad (8)$$

Here, n_g is a scaling factor (usually taken to be 3 if not specified differently), μ the monthly mean values from the observations and the models at all latitudes or for all months (N), and σ_{obs} the standard deviation of the measurements. Note that n_g and σ_{obs} are often not straightforwardly determined, and therefore involve subjective choices. This needs to be taken into account when interpreting grades from this metric, as emphasized by Waugh and Eyring [2008] and Grewe and Sausen [2009].

3.2.3. Combining Pattern and Mean State Metrics

[35] The final grade (G_{tot}) of model performance for each diagnostic is then defined by the linear combination of the skill score (S ; see equation (7)) and the grading of the mean (g_m ; see equation (8)):

$$G_{tot} = (S + g_m)/2. \quad (9)$$

[36] The G_{tot} of the different diagnostics are then listed in a summary matrix (Figure 19). We will derive total grades only for the diagnostics 1, 2, and 5 to 8 of Section 3.1, since these diagnostics are easy to define or more established in the literature than diagnostics 3, 4, and 9. The latter diagnostics therefore have to be seen as ‘experimental’ diagnostics.

4. Results

4.1. Dynamical Structure of the Extratropical UTLS

4.1.1. Zonal Mean Zonal Wind at 200 hPa

[37] The zonal mean zonal wind field is used to validate the representation of the thermal structure of the models, and therefore the basic dynamical state of the models’ atmospheres. For this diagnostic, monthly zonal mean wind fields averaged over the period 1979–1999 and for JJA (June–July–August) and DJF (December–January–February) are compared between the model simulations and ERA-40 reanalyses. NCEP reanalyses are also included for further comparison with ERA-40 and the models.

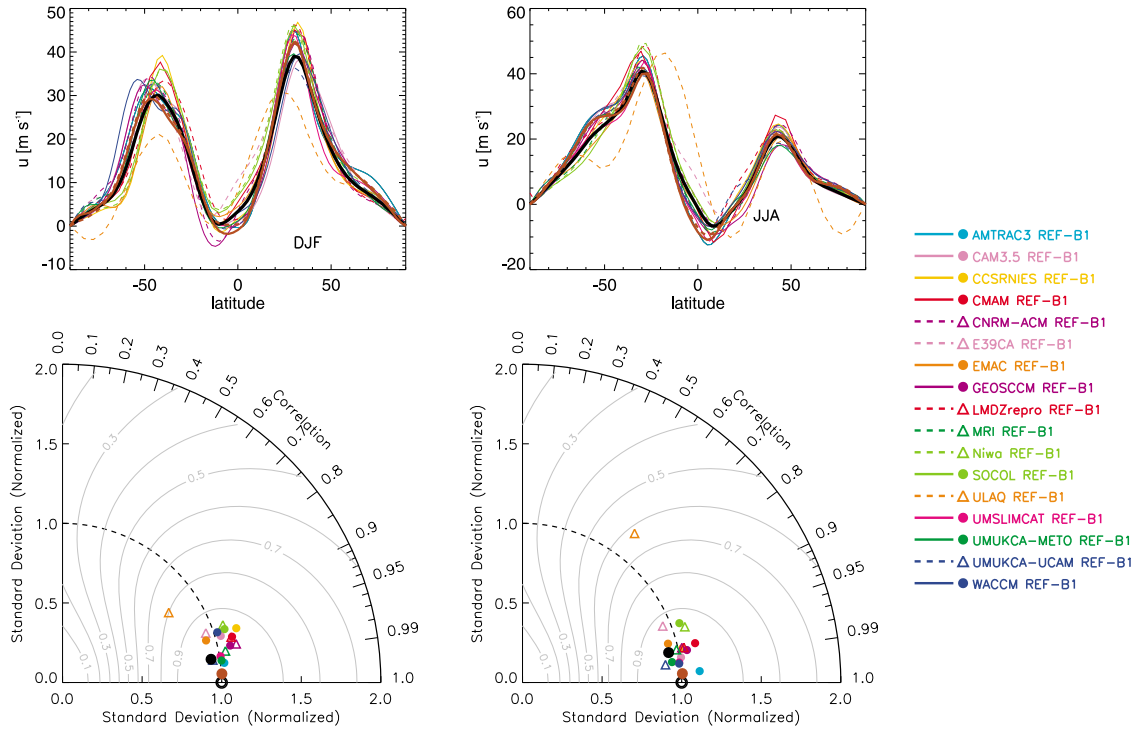


Figure 3. (top) Zonal mean zonal wind and (bottom) corresponding Taylor diagrams at 200 hPa for (left) DJF and (right) JJA. Brown solid line represents ERA-40 data, brown dashed line and brown dot represent NCEP data, and black solid line is the multimodel mean.

[38] Figures 3, 4, and 5 illustrate that the models represent the strength and latitudinal behavior of the observed zonal mean zonal wind in a realistic way. This is to be expected since the zonal mean wind fields have been used extensively as a diagnostic to help improve gravity wave parameterizations in model development. ULAQ is the only model that shows clear deficiencies in resolving the latitudinal structure, especially during JJA. This lack of realism is also expressed in the Taylor diagrams by very low latitude-by-latitude correlation and skill values. ULAQ also scores very low in the climatological mean state metric, with 0.5 during DJF and 0.3 during JJA. The low performance of ULAQ might be attributable to the very low resolution of the model and the quasi-geostrophic dynamical core characterizing this model. In the mean state metric, the SOCOL-based models score slightly lower than the multimodel mean during both DJF and JJA.

[39] The tight correspondence between NCEP and ERA-40 (the skill of NCEP is 0.98), with the models lying much farther away from the reference point, indicates that the reanalyses are consistent with each other and that the models may still have room for improvement. For example, several models displace the tropospheric ‘eddy-driven’ jet in the SH summer (DJF) when compared to the observations.

[40] The total grading values (G_{tot}) obtained in Figures 4 and 5 for the two seasons are averaged and listed in the summary matrix (Figure 19).

4.1.2. Seasonal Cycle of LMS Mass

[41] The seasonal cycle of the LMS mass is a basic test of the response of the atmosphere to a combination of direct radiative forcing through changes in UTLS temperatures as well as of dynamical forcing through the wave-driven Brewer-Dobson

circulation, and represents an integrated measure for the tropopause behavior. Stratospheric mass variations due to seasonal tropopause height variations can contribute to stratosphere-troposphere exchange [Appenzeller *et al.*, 1996]. This exchange transports ozone, reactive nitrogen, and other species into the troposphere, where it affects the tropospheric ozone budget and with it air quality. We test here the realism of the seasonal variations of the total LMS mass by comparing them to the NCEP reanalyses using a method similar to that of Appenzeller *et al.* [1996]. The LMS mass is defined as the mass of the stratospheric region that lies between the thermal tropopause, calculated using the WMO definition [World Meteorological Organization, 1957], and the 100 hPa pressure surface. The thermal tropopause is derived from monthly zonal mean temperature fields averaged over a time period between 1990 and 1999. Note that the 100 hPa pressure level, unlike the 380 K potential temperature level, does not reflect the seasonal shifts in the upper boundary of the LMS. The results are shown in Figure 6.

[42] In the NH, most models show a very high skill (with values larger than 0.9) in reproducing amplitude and phase of the seasonal cycle of the LMS mass from the NCEP reanalyses. One exception is LMDZrepro which only scores 0.62. LMDZrepro’s variability is too low (with a standard deviation of about 0.5), however the model captures the seasonal evolution (correlation of 0.95). There are also quite a few models that have difficulty in simulating accurate mean values of the LMS mass as compiled in Figure 7. UMUKCA-METO and UMUKCA-UCAM exhibit too large LMS masses, indicating an average tropopause pressure that is too high. CCSRNIIES, CNRM-ACM, EMAC, Niwa-SOCOL, SOCOL, and ULAQ have smaller LMS mass values than

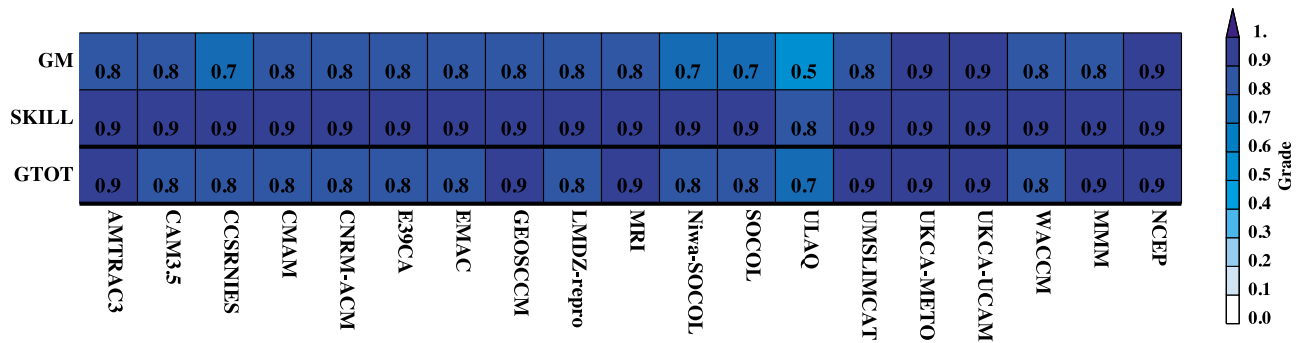


Figure 4. Metric table for the zonal mean wind at 200 hPa (DJF). ‘MMM’ denotes the multimodel mean. For convenience the colors are labeled by the lower limit of their range.

NCEP, indicating generally too low tropopause pressures. These findings are consistent with the evaluation of the annual mean tropopause heights by *Gottelman et al.* [2010], which show that the SOCOL-based (UMUKCA-based) models exhibit too low (high) tropopause pressures in both the tropics and the extratropics.

[43] In the SH, the models’ overall performance is worse than in the NH. The skill based on the correlative metrics lies around 20–40% lower than in the NH for all models, with particular deficiencies for CAM3.5, CCSRNIES, GEOSCCM, ULAQ, UMSLIMCAT, and WACCM. The Taylor diagram reveals that almost all models exhibit standard deviations that are too large, which moves them further away from the reference point (note the different radial axis scale in the Taylor diagrams in Figure 6). The following models have major deficiencies in representing the mean values (see Figure 8): CNRM-ACM, CCSRNIES, UMUKCA-METO, and UMUKCA-UCAM. The differences between SH and NH are likely due to the much less pronounced seasonality seen in the SH, but may also stem from the fact that the reanalyses the models are being compared to are less consistent and therefore less reliable in the SH than in the NH [*Schoeberl, 2004*].

[44] The total grading values (G_{tot}) obtained in Figures 7 (for the NH) and 8 (for the SH) are averaged and listed in the summary matrix (Figure 19). The models that perform the best (showing total scores [G_{tot}] larger than 0.8) are AMTRAC3, CMAM, E39CA, GEOSCCM, and MRI, which are the models that also reach the highest scores in the NH.

4.1.3. Tropopause Pressure Anomalies

[45] The extratropical tropopause pressure is a basic measure of the vertical structure in a model. We focus here on interannual anomalies in the monthly and zonal mean tropopause pressure that yield insight into the models’ abilities to respond to forcing of the climate system. While the use of this diagnostic has proven to be useful in the tropics [*Gottelman et al., 2010*], we may not necessarily expect the same strong connection between sea surface temperatures and the tropopause pressure in the extratropics. This diagnostic has therefore to be seen as more explorative, for which reason we do not use it as a metric in the final evaluation.

[46] The tropopause is calculated using the WMO-definition and averaged over 40°N–60°N and 40°S–60°S, respectively. The analysis is based on monthly mean temperature fields. The models are compared to five different analyses: ERA Interim, NCEP2, JRA25, and ERA-40.

[47] Although the models seem to reproduce the seasonal cycle of tropopause pressure well in the NH (based on the diagnostic for the LMS mass in Section 4.1.2), they show more problems in representing interannual variability. This can be seen from Figure 9. CNRM-ACM has an unrealistically large interannual variability and a low tropopause pressure, as also has been noted in the corresponding analysis in the tropics [*Gottelman et al., 2010*]. The excessive variability is due to a large signal from volcanic aerosol heating (note the correspondence of anomalies with recent major volcanic events). CCSRNIES, EMAC, ULAQ and WACCM

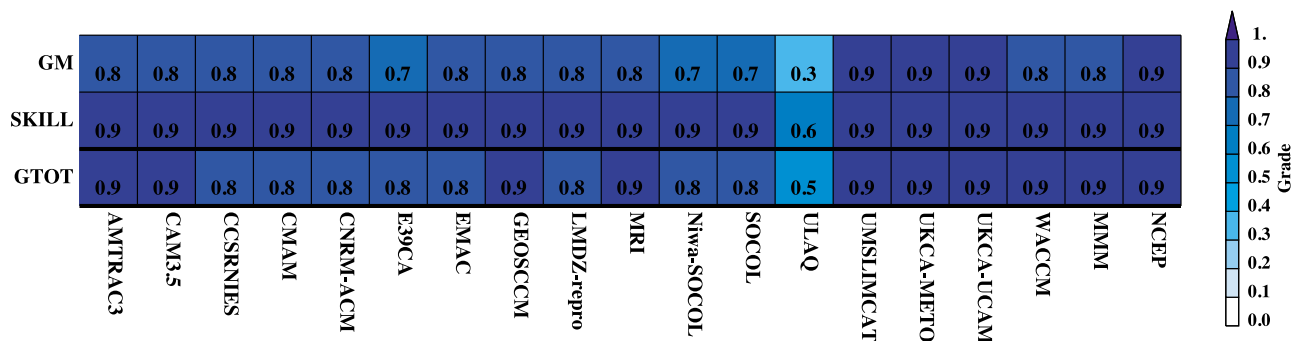


Figure 5. Same as Figure 4 but for JJA.

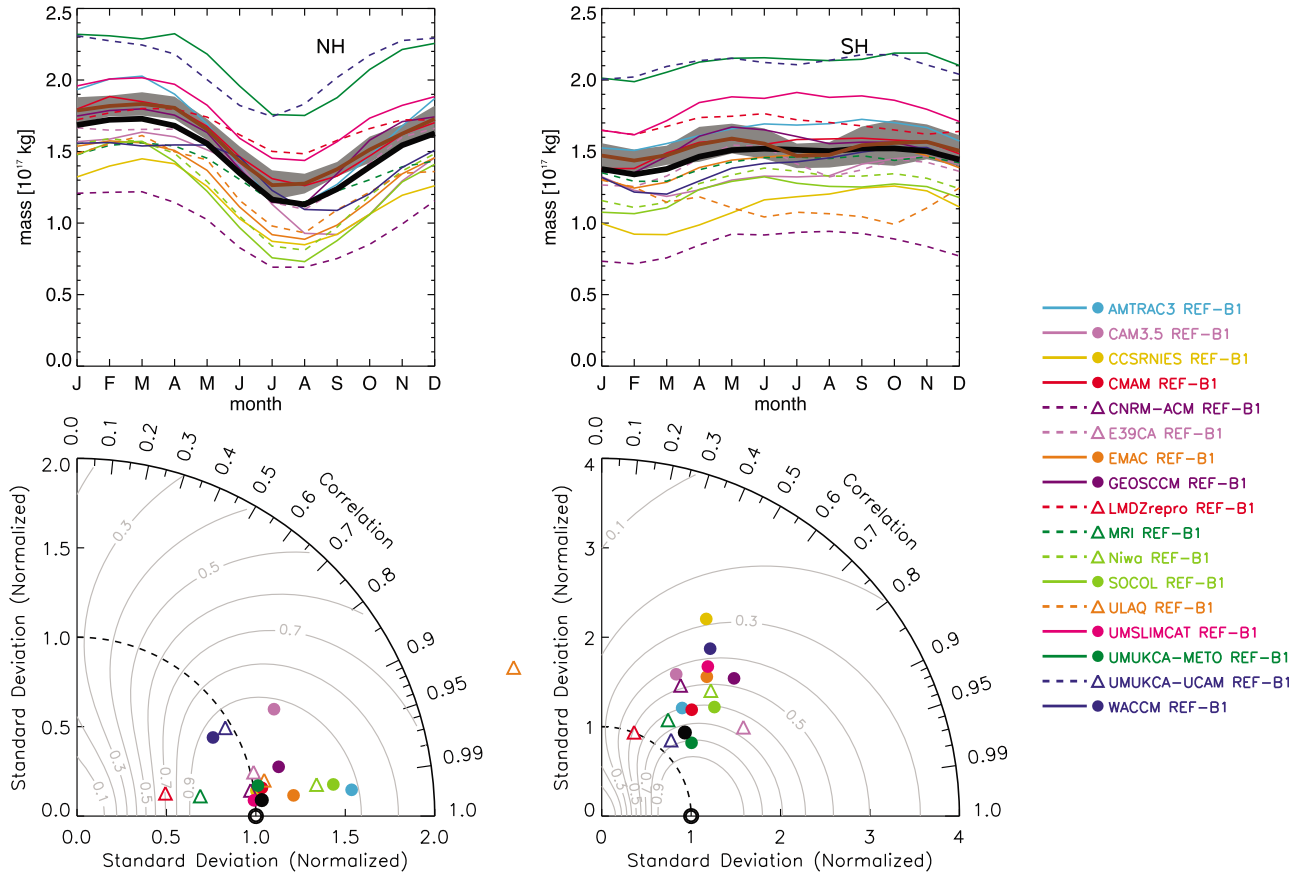


Figure 6. (top) Seasonal cycle of LMS mass following *Appenzeller et al.* [1996] and (bottom) corresponding Taylor diagrams of model performance for (left) NH and (right) SH. Black line represents the multimodel mean, and brown line and gray shading denote NCEP mean with 2σ uncertainty. Note the different scale on the radial axis in the SH.

perform worst among the models due to both too high or low mean values and very small correlation with the observed variability structure. The low correlation is most obvious during years that show volcanic events, where these models do not show the expected drops in pressure.

[48] In the SH, the models simulate the interannual variability somewhat better, except for CNRM-ACM which exhibits a too large interannual variability and a too low tropopause pressure as found also in the NH. CCSRNIES, MRI, ULAQ, and WACCM have a negative bias in the mean tropopause pressure, and ULAQ shows the worst correlation with the reanalyses.

4.1.4. Tropopause Inversion Layer

[49] A strong temperature inversion with a depth of a few kilometers and located just above the tropopause (also called the tropopause inversion layer, TIL), has been extensively investigated using high-resolution radiosondes [Birner et al., 2002; Birner, 2006; Bell and Geller, 2008] and Global Positioning System (GPS) Radio Occultation (RO) data [Randel et al., 2007; Grise et al., 2010]. The TIL is characterized by a sharp and strong maximum in static stability ($N^2 = \frac{g}{\theta} \frac{d\theta}{dz}$). The presence of the TIL is believed to be important for the impact of cross-tropopause exchange on chemical tracer distributions, wave-breaking and wave-generation [Miyazaki et al., 2010a], and for the dynamical coupling between the stratosphere and the troposphere.

[50] N^2 has been calculated for 9 different models for which the necessary instantaneous data fields (i.e. on model levels) were available and compared to the COSMIC (Constellation Observing System for Meteorology, Ionosphere, and Climate) GPS-RO data. Three years of data were used between 2006 and 2009, with up to 3000 profiles per day. The analysis is performed in tropopause coordinates using the tropopause pressure as reference (p_{TP}) and with height $z = -H \ln(p/p_{TP})$, where H is a scale height of 8 km. The observed TIL is computed using both data at full vertical resolution and data only at CCMVal-2 standard levels, so as to ensure a fair comparison between the high resolution observations and the lower resolution model fields. The use of degraded observations reduces differences due to the models' low vertical resolution, and the remaining differences may then be attributed more likely to missing processes in the models.

[51] Zonal mean cross-sections and tropical profiles of N^2 are discussed in detail by Gettelman et al. [2010]. Here, we discuss in addition how models perform in simulating N^2 profiles at two latitude bands, representing the Northern Hemisphere TIL in winter and summer (Figure 10). In general, the models seem to be capable of reproducing the qualitative structure and seasonality of the TIL. The TIL has a weaker maximum during winter and a stronger maximum

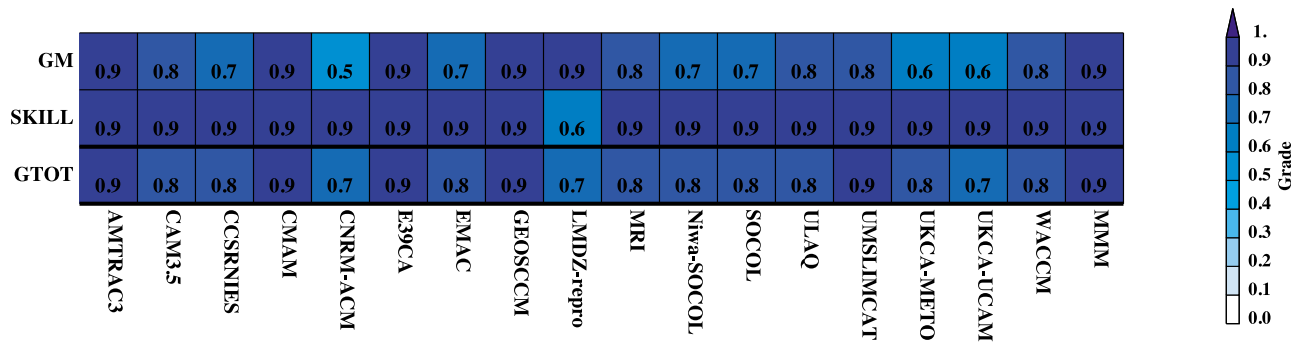


Figure 7. Same as Figure 4 but for LMS mass in the NH.

during summer, which increases also with latitude [Birner, 2006; Randel *et al.*, 2007].

[52] It can also be seen that maximum values of simulated N^2 are comparable to or larger than those derived from degraded GPS data. However, they are always weaker than those computed from full-level GPS data unless vertical resolution is sufficiently high as seen for the high-resolution version of WACCM with a vertical resolution of 300 m in the UTLS region. It is also evident that the location of maximum N^2 in the CCMVal-2 models is found always at somewhat greater distances from the tropopause and to be broader than in the full GPS data, but closer to that seen in the degraded GPS data. Again, the high-resolution WACCM version yields better results with a maximum N^2 location closer to the observed one, although the maximum is still too broad. Some of the shift in the N^2 maximum can therefore be explained by the limited resolution of the CCMs, and does not necessarily mean that they misrepresent the processes determining the TIL structure. Another more detailed comparison between a high-resolution (T213L256) and a low-resolution (T41L32) version of a global circulation model (GCM), which supports this conclusion, is given by Miyazaki *et al.* [2010b]. They show that the high-resolution version of their model (given all other model settings to be equal) was capable of reproducing the fine-scale structure and seasonality of the TIL much better than the low-resolution version, with the maximum in N^2 being more realistic and located closer to the tropopause.

[53] The above comparisons indicate that the CCMs are qualitatively reproducing the TIL, but underestimate the strength of the TIL quantitatively, most likely due to their

limited vertical resolution. A too weak TIL is likely to result in too weak potential vorticity gradients across the tropopause, which in turn may lead to too strong transport across the tropopause and may also alter wave-propagation into the stratosphere or wave-generation in the tropopause region.

4.2. Transport and Mixing Within the Extratropical UTLS

4.2.1. Seasonal Cycle of Tracers at 100 and 200 hPa

[54] The large-scale Brewer-Dobson circulation consists of two main branches. The deeper branch is driven mainly by planetary wave breaking in the stratosphere and transports aged stratospheric air into the LMS. The shallow branch is driven by the breaking of both synoptic scale and planetary waves above the subtropical jet and transports (and ultimately mixes) younger tropical air masses to higher latitudes. Both transport processes exhibit a seasonally varying strength, and determine the chemical background composition of the LMS. It is crucial for CCMs to capture the relative strength and seasonality of these processes, since they determine the distribution of O_3 and H_2O in the LMS (which through radiative heating have a strong impact on the temperature distribution and therefore on winds), and also the monthly input of stratospheric ozone into the troposphere.

[55] The models' representation of these large-scale transport and mixing processes, which take place on time-scales of weeks to a couple of months, is evaluated here using the seasonal cycles in O_3 , HNO_3 , and H_2O at 100 and 200 hPa averaged between 40° and 60° N and S, respectively. While O_3 and HNO_3 are expected to exhibit similar seasonal cycles since their sources in the UTLS are mostly

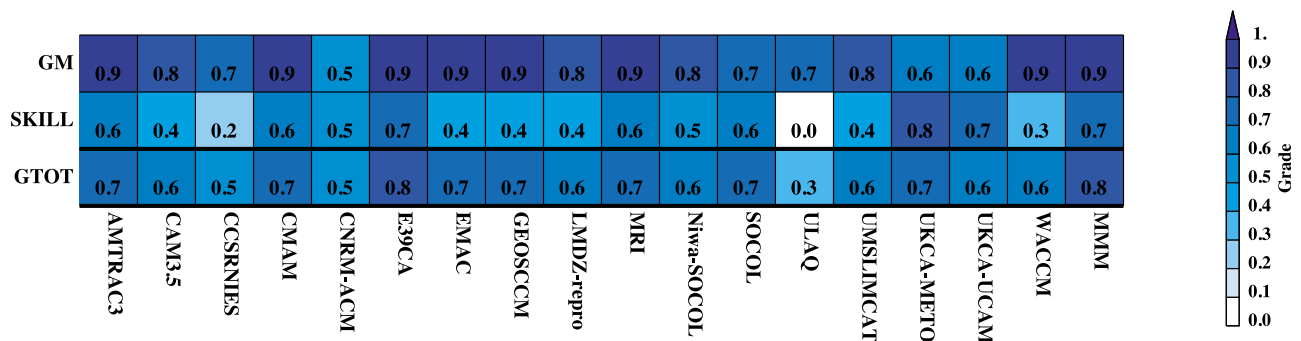


Figure 8. Same as Figure 4 but for LMS mass in the SH.

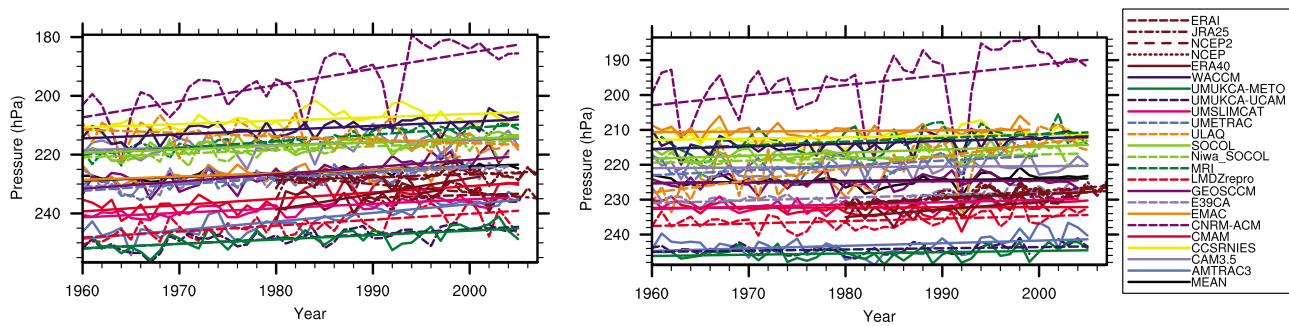


Figure 9. Extratropical tropopause pressure variability for (left) SH and (right) NH.

stratospheric, H_2O is a tropospheric tracer in the UTLS (since the contribution of CH_4 -oxidation to the H_2O budget is small) and gives insight into a possible tropospheric influence. HNO_3 is further affected by chemistry and microphysics, which may cause some differences to the structure seen in the O_3 seasonal cycle. The monthly mean zonal mean tracer fields from 2000–2006 are compared to observations obtained by MIPAS between 2004 and 2008, MLS during 2006, and the ACE-FTS between 2004 and 2008.

[56] The top two rows in Figures 11 and 12 show the results for the 100 hPa level with the corresponding Taylor diagrams in the NH and SH, respectively. In the NH, O_3 is relatively well represented in all the models despite a tendency to overestimate the mean (not shown) and the amplitude (i.e. standard deviation) of the seasonal cycle relative to MIPAS observations. The models' variability is also too strong when compared to MLS observations; however the correlation improves slightly. The Taylor diagram also reveals slightly lower correlation values than average for CAM3.5, ULAQ, UMUKCA-UCAM, and WACCM. The seasonal cycle of HNO_3 mostly confirms this behavior, with the exception of UMUKCA-METO, which exhibits a very low correlation with MIPAS satellite observations. The behavior in the seasonal cycle of H_2O is similar to the tropics [see Gettelman *et al.*, 2010], pointing toward a strong connection between the tropics and the

extratropics. The performance of the models therefore strongly depends on their ability to represent tropical processes such as dehydration and the seasonal strength in the meridional mixing between the tropics and the extratropics. Models that score low in the tropical H_2O diagnostic [Gettelman *et al.*, 2010] indeed score low also in the diagnostic presented here. The too large amplitude in O_3 may also have its origin in the tropics, which is supported by the finding of Gettelman *et al.* [2009] that most of the CCMVal-1 models' O_3 in the tropics increases too quickly at and above the tropopause. This bias is somewhat less pronounced in the CCMVal-2 models, but several outliers still exist. The seasonal cycles in the SH show generally smaller amplitudes, reflecting the weaker influence of the Brewer-Dobson circulation. The models generally show the same behavior, however they tend to overestimate the mean O_3 values.

[57] The results for the 200 hPa level are shown in the two bottom rows in Figures 11 and 12. At 200 hPa in the NH, the O_3 seasonal cycle is well represented in almost all the models. However, the mean values and amplitudes tend to be rather low compared to those in the observations. CNRM-ACM, Niwa-SOCOL, and SOCOL score worst; these models show, apart from too low amplitudes, also relatively low month-by-month correlations in comparison with the MIPAS observations. HNO_3 again shows a consistent behavior in almost all the models. The low mean values in both O_3 and HNO_3 can be explained by too much

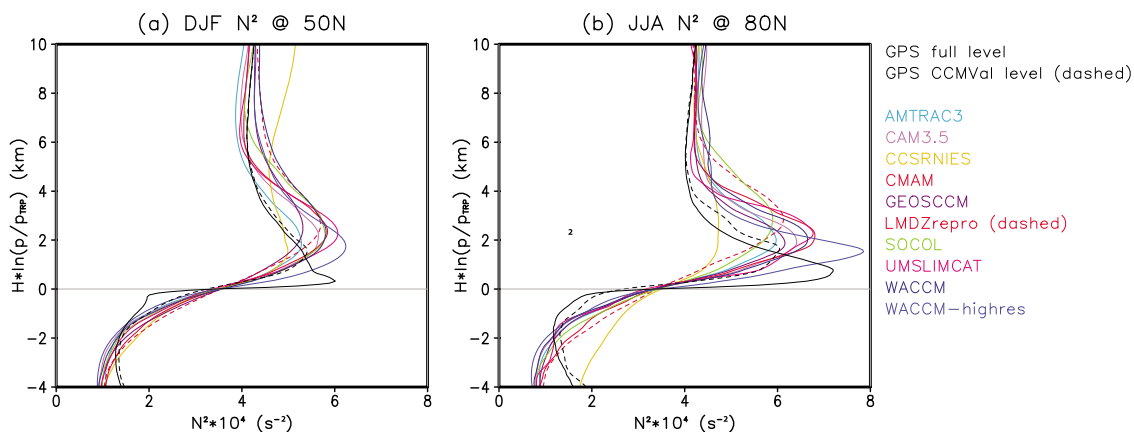


Figure 10. Vertical profiles of N^2 in models and observations at (a) 50°N during DJF and (b) 80°N during JJA.

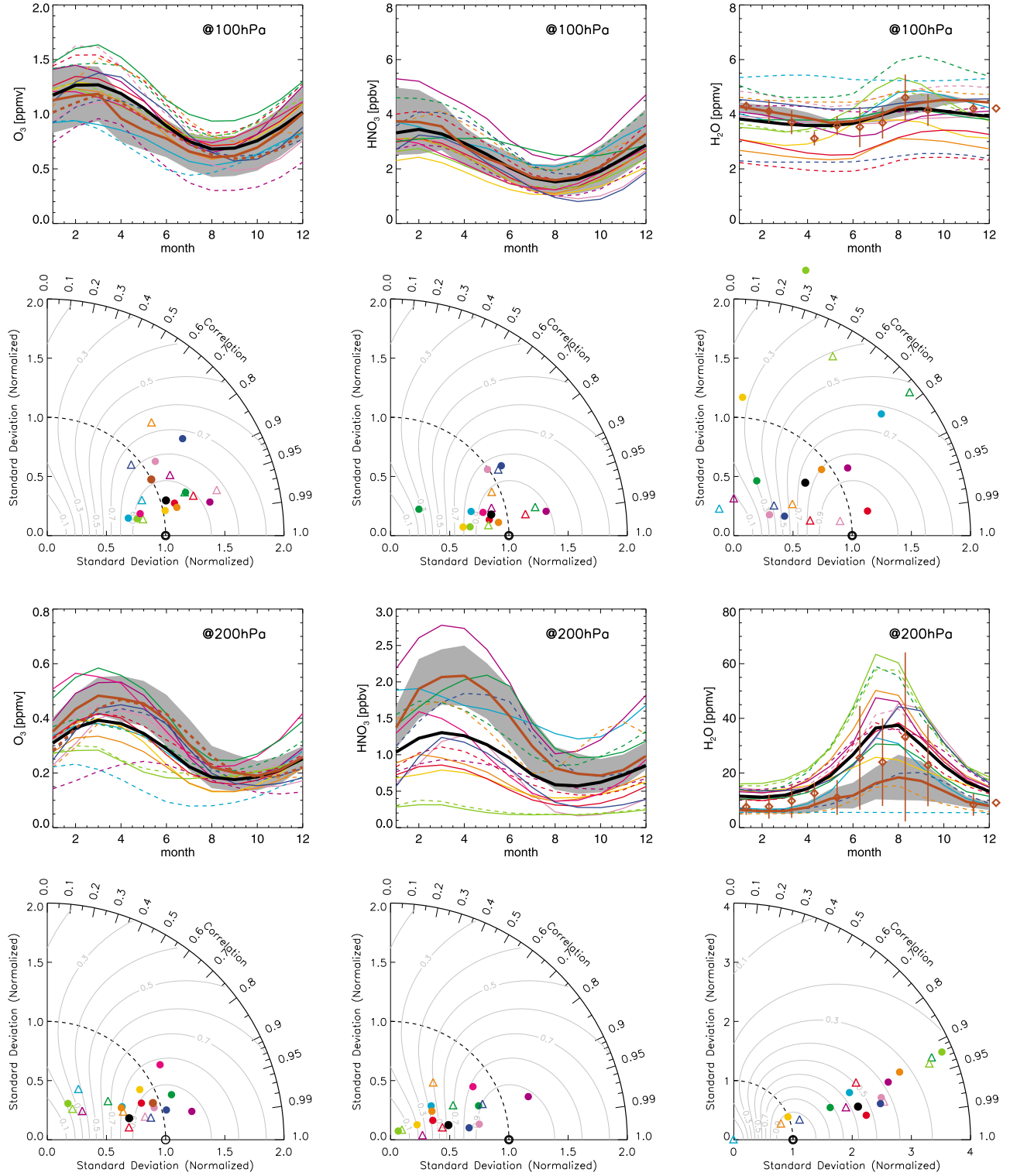


Figure 11. Seasonal cycles in monthly mean (left) O₃, (middle) HNO₃, and (right) H₂O between 40°N and 60°N and corresponding Taylor diagrams at (top two rows) 100 hPa and (bottom two rows) 200 hPa for different models (color code; see Figure 6 legend) and compared to MIPAS satellite data (brown solid lines) $\pm 1\sigma$ (gray shading) over the years 2004–2008. In addition to the MIPAS data, MLS O₃ data (brown dashed line and brown dots) and ACE-FTS H₂O data (brown diamonds) are also shown. The multimodel mean is denoted in black.

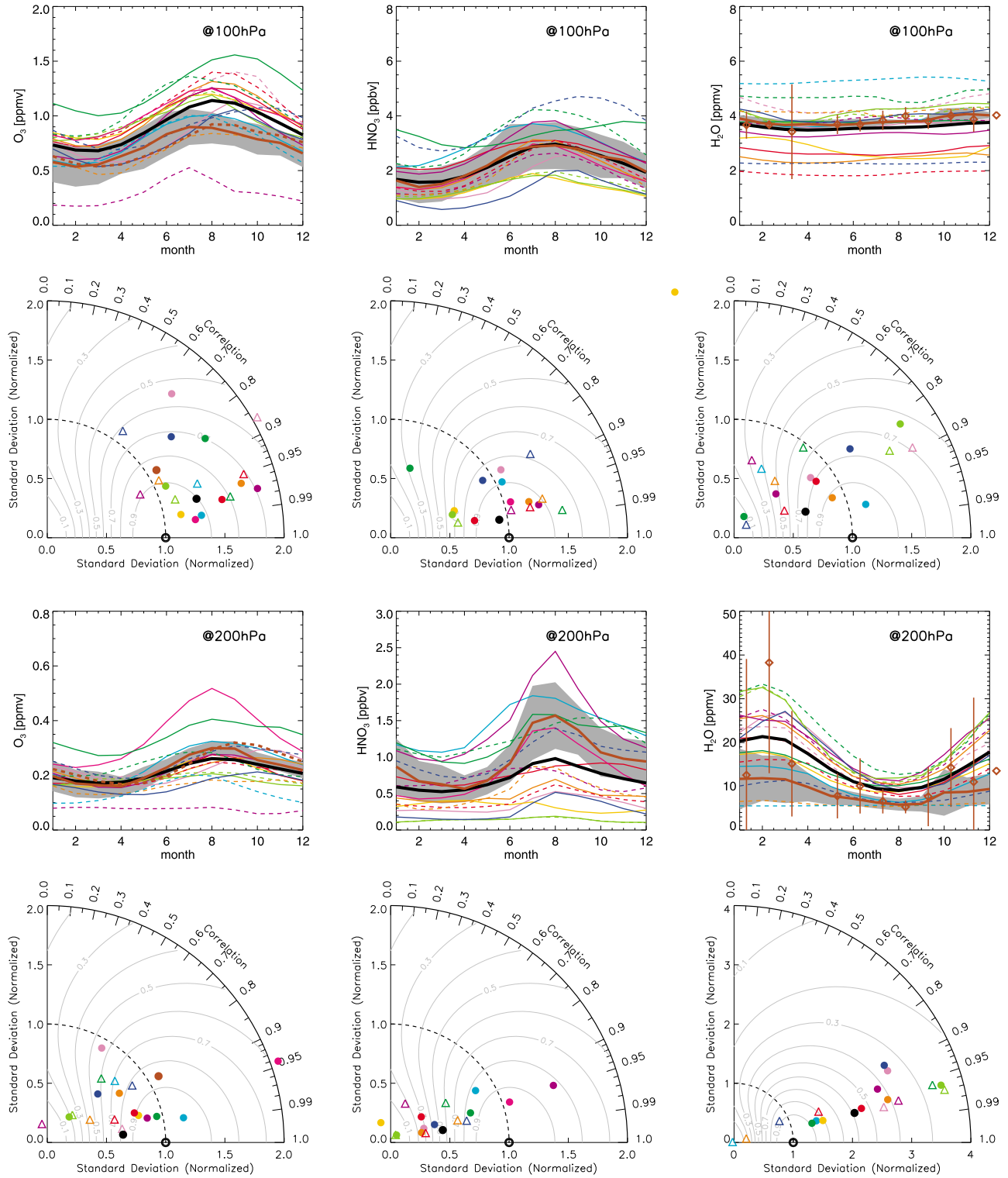


Figure 12. Same as Figure 11 but for latitudes between 40°S and 60°S.

transport across the subtropical and extratropical tropopause. This is reflected also in too large amplitudes (standard deviations) in the H_2O seasonal cycle, the tropospheric tracer which is most sensitive to mixing due to its exponential decrease across the tropopause. Tropospheric influence seems to be particularly high during late summer and

autumn. The lack of a sophisticated tropospheric chemistry in most models may also contribute to some of the observed differences. As the analysis is done on fixed pressure levels, the model biases could in principle originate from biases in the tropopause altitude. However, this does not seem to be the case. MRI for example exhibits a too low tropopause,

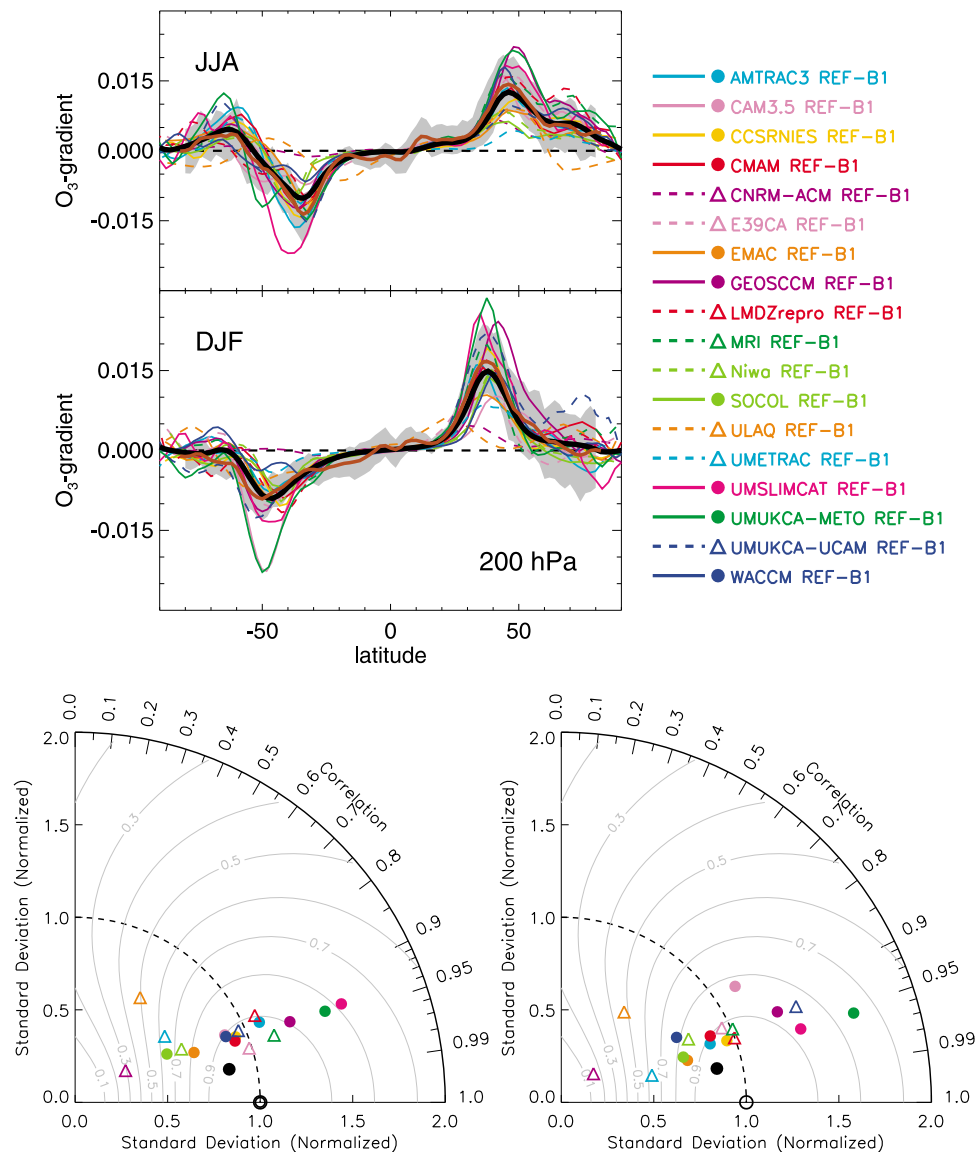


Figure 13. Meridional gradient in O_3 at 200 hPa and corresponding Taylor diagrams for (top and bottom left) JJA and (middle and bottom right) DJF. Brown thick lines and gray shading show MLS observations averaged over 2006–2008 with 1σ uncertainty.

but also too strong mixing, while UMSLIMCAT exhibits a too high tropopause, but not enough mixing (inferred from too high O_3 , since H_2O is not available). SOCOL and Niwa-SOCOL both are too diffusive, possibly due to their semi-Lagrangian transport scheme. In the SH, the observed seasonal cycles of all the three tracers at 200 hPa show smaller amplitudes consistent with the finding on the 100 hPa level. Again, the models' means and amplitudes (standard deviations) in O_3 and HNO_3 are shifted to values smaller than expected from the observations with H_2O indicating too strong cross-tropopause transport or too high tropopause temperatures. Note that there is some evidence that the seasonal cycle in MIPAS H_2O at 200 hPa exhibits a smaller amplitude than other satellite observations like HALOE and MLS. Indeed, comparison with the ACE-FTS measurements, which yielded a good agreement with high-resolution aircraft

measurements [Hegglin *et al.*, 2008], indicates that MIPAS H_2O might be somewhat low especially during summer on the 200 hPa level and in both hemispheres, a retrieval or instrument issue which is currently under investigation. However, the large noise and standard deviations in the ACE-FTS data imply that the sampling from the ACE-FTS is not sufficient to determine the seasonal cycle of H_2O accurately. The discrepancies between the two satellite observations reveal how problematic H_2O measurements in the UTLS from space are, which is mainly due to the high variability and large spatial and temporal gradients in H_2O found in the UTLS. At the moment, the metrics presented here are therefore not defined accurately. Additional measurements with higher (spatial and temporal) resolution and higher accuracy will be needed to resolve this issue and to gain more confidence in this metric in the future. Comparison

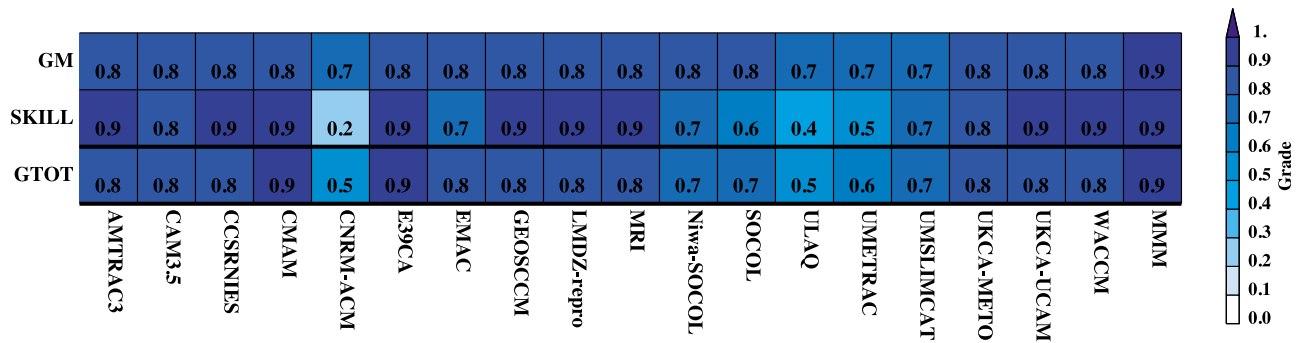


Figure 14. Same as Figure 4 but for meridional gradient in O_3 at 200 hPa for JJA.

with MLS O_3 on both pressure levels and for both hemispheres however indicates good agreement between MLS and MIPAS.

[58] For this diagnostic we derive two different grades for each model. One grade is based on the O_3 seasonal cycle, and calculated as the average over all mean grades (g_m) and skill scores obtained for both pressure levels and hemispheres. The other grade is based on the H_2O seasonal cycle, calculated as the average of all skill scores obtained for both pressure levels and hemispheres. We do not include a grade for the mean value of H_2O , since it is already used as a metric in the vertical profiles (see Section 4.2.4). The model grades are then listed in the summary matrix (Figure 19).

4.2.2. Meridional Tracer Gradients at 200 hPa

[59] Useful information on mixing barriers and therefore the degree of isolation and chemical distinctness of different regions such as the tropics and the extratropics is provided by the sharpness of meridional gradients of long-lived species. Here we use the meridional gradient in O_3 at 200 hPa (which is long-lived compared to the transport time scales in this region). We use seasonal means for JJA and DJF derived from monthly mean zonal mean O_3 fields from all models and compare them to a multiyear seasonal climatology derived from MLS data (averaged over 2004–2008). Ideally one would examine the gradient of the mode of the probability density function rather than the mean [Shepherd, 2002], as this provides a more robust representation of the tracer gradient. However, this would require 3D instantaneous data which are not available for all the models.

[60] The models generally reproduce the meridional gradients in both JJA and DJF well (Figure 13), which implies

that they can reproduce the separation between the tropical UT and the extratropical LMS. In JJA (Figure 13, bottom left), the correlations are mostly higher than 0.9 except for CNRM-ACM, ULAQ and UMETRAC, which show correlations between 0.5 and 0.8. However, there is a substantial spread in the models in terms of standard deviations, resulting in decreased skill scores (also see Figure 14). Too low amplitudes in the meridional gradient are found in CNRM-ACM, EMAC, the SOCOL-models, ULAQ and UMETRAC, and too high amplitudes in UMSLIMCAT and UMOUKCA-METO, diminishing their skill score to values below 0.85. In DJF (Figure 13, bottom right, and Figure 15), the models perform slightly worse, especially CNRM-ACM, ULAQ, UMETRAC and UMOUKCA-METO.

[61] A relation between this diagnostic and the zonal mean zonal wind might be expected, however this seems to be true only for ULAQ, which shows low grades for both the zonal mean zonal wind and for the meridional gradient. It is noteworthy that the multimodel mean produces in both seasons the most realistic picture of the meridional ozone gradient with skills reaching values of 0.94.

4.2.3. Normalized CO in Tropopause Coordinates

[62] To evaluate the representation of tropospheric influence on the background LMS in the models, and to distinguish between transport across the extratropical tropopause on short time scales and transport from the tropics and subtropics on longer time scales, we use CO which has an approximate lifetime of 3 months in the LMS. In the middle stratosphere above $\Theta = 500$ K, CO is nearly constant with an observed background value of 10–15 ppbv [Flocke et al., 1999], due to the chemical equilibrium between methane

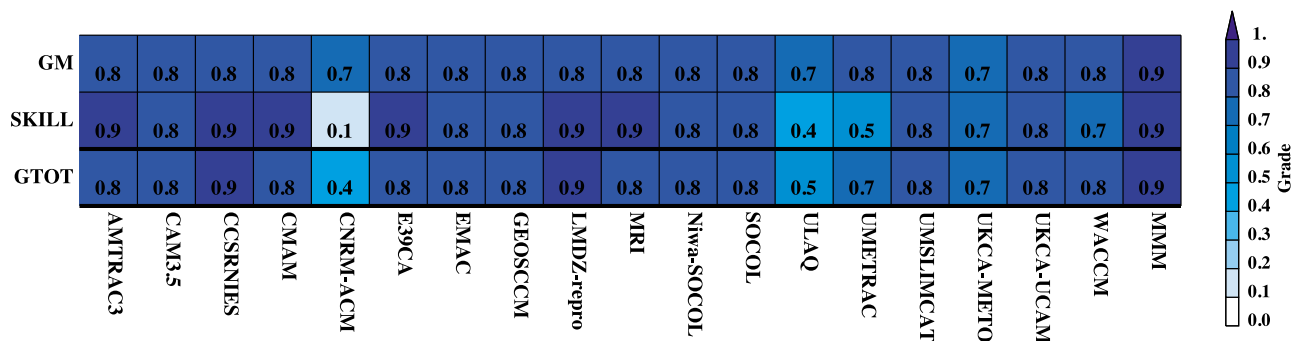


Figure 15. Same as Figure 4 but for meridional gradient in O_3 at 200 hPa for DJF.

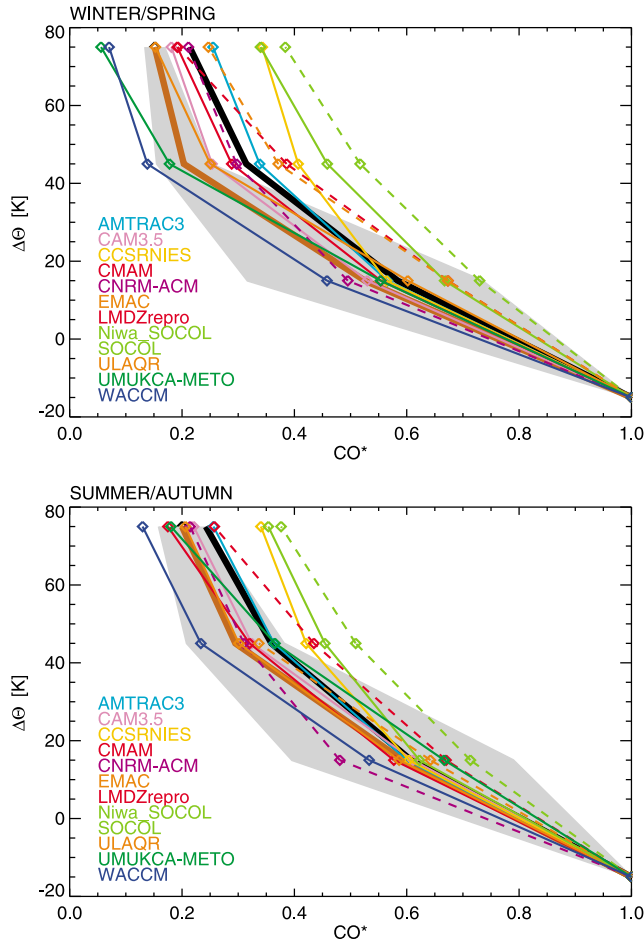


Figure 16. Profiles of CO^* (normalized CO) for winter/spring and summer/autumn in layers of $d\Theta = 30$ K from the dynamical tropopause. SPURT aircraft measurements are denoted in brown with $\pm 1\sigma$ standard deviation indicating interannual variability (gray shading). The different models are given in color. Black is the multimodel mean.

and CO oxidation. Any excess CO must then originate from the troposphere.

[63] To examine the coupling between the LMS and the extratropical troposphere, CO was evaluated in tropopause coordinates, expressed in potential temperature units relative to the potential temperature of the 2 PVU surface ($d\Theta$) as applied to the SPURT data set [Hoor *et al.*, 2004, 2005]. Key results from Hoor *et al.* [2004, 2005] are: (i) The coupling to the local troposphere drops below 25% over the lowest 30 K above the 2 PVU tropopause. (ii) Higher above the tropopause ($d\Theta > 30$ K), influence of the subtropical troposphere accounts for the background CO in the LMS, which varies with season. (iii) The largest differences are found between winter/spring and summer/autumn.

[64] In order to test if the CCMVal-2 models represent these characteristics in the CO distribution, instantaneous model output for the year 1995 was sampled within the SPURT measurement domain (30°N – 80°N , 20°W – 10°E). The year 1995 has been chosen for comparison since more models provided instantaneous data during the 90's than during the SPURT period. We assume that the choice of the

model year has a negligible impact on the results of this evaluation. Data were analyzed in layers of 30 K relative to the 2 PVU surface (represented by the centered layer means at -15 , 15 , 45 , and 75 K in Figure 16). The tropospheric fraction of CO in the stratosphere (CO^*) is determined by

$$\text{CO}^* = (\text{CO} - \text{CO}_{\text{strat}}) / (\text{CO}_{\text{trop}} - \text{CO}_{\text{strat}}) \quad (10)$$

where CO_{strat} is the stratospheric background value of each individual model defined as the mean value within the 500–600 K layer, and CO_{trop} is the mean value for the layer between -30 and 0 K below the tropopause. The normalization using the factor $1/(\text{CO}_{\text{trop}} - \text{CO}_{\text{strat}})$ accounts for the varying boundary specifications of CO in the models, which we do not want to test here. Models that did not provide instantaneous fields were not included in the comparison.

[65] Two properties were tested and graded as follows.

[66] 1. The abundance of CO^* between 30 and 60 K above the tropopause as a measure for tropospheric influence. A model was given a grade $W1$ of 3, 2, 1, 0 if the difference between the SPURT observations and the model was $<1\sigma$, $<2\sigma$, $<3\sigma$, and $>3\sigma$ of the observational standard deviation, respectively.

[67] 2. The decreasing coupling to the local 2 PVU tropopause found in the layers 0–30 K and 30–90 K above the tropopause as represented by the different gradients in CO^* in the respective layers. A model was given a grade $W2$ following the same scheme as in (1) but comparing the ratio of the gradients in CO^* at the 60 K and 0 K levels obtained for the model and the observations.

[68] High values for both weights (Table 3) therefore indicate a good separation from the extratropical troposphere and mainly weak influence from the subtropics (as seen for UМУKCA-METO and EMAC). Low values for $W1$ (abundance), but high values for $W2$ (separation) reflect too much tropospheric CO (CO^*) in the LMS, but the transition from the local troposphere to the LMS occurs correctly within $d\Theta = 0$ –30 K (AMTRAC3 and CCSRNIIES). Low values for both $W1$ and $W2$ indicate that the coupling to the extratropical tropopause extends too deep into the stratosphere (LMDZrepro and Niwa-SOCOL during winter/spring), leading to an unrealistic tropospheric contribution

Table 3. Grading for the Normalized CO Gradient in Tropopause Coordinates

	Winter/ Spring		Summer/ Autumn		TOTAL ($\Sigma W/12$)
	W1	W2	W1	W2	
AMTRAC3	1	3	3	3	0.83
CAM3.5	2	3	3	3	0.92
CCSRNIIES	0	3	2	3	0.67
CMAM	2	3	3	3	0.92
CNRM-ACM	2	3	3	3	0.92
EMAC	3	3	3	3	1.00
LMDZrepro	0	1	2	3	0.50
Niwa-SOCOL	0	1	1	3	0.42
SOCOL	0	2	2	3	0.58
ULAQ	0	2	3	3	0.67
UМУKCA-METO	3	3	3	3	1.00
WACCM	2	3	3	3	0.92

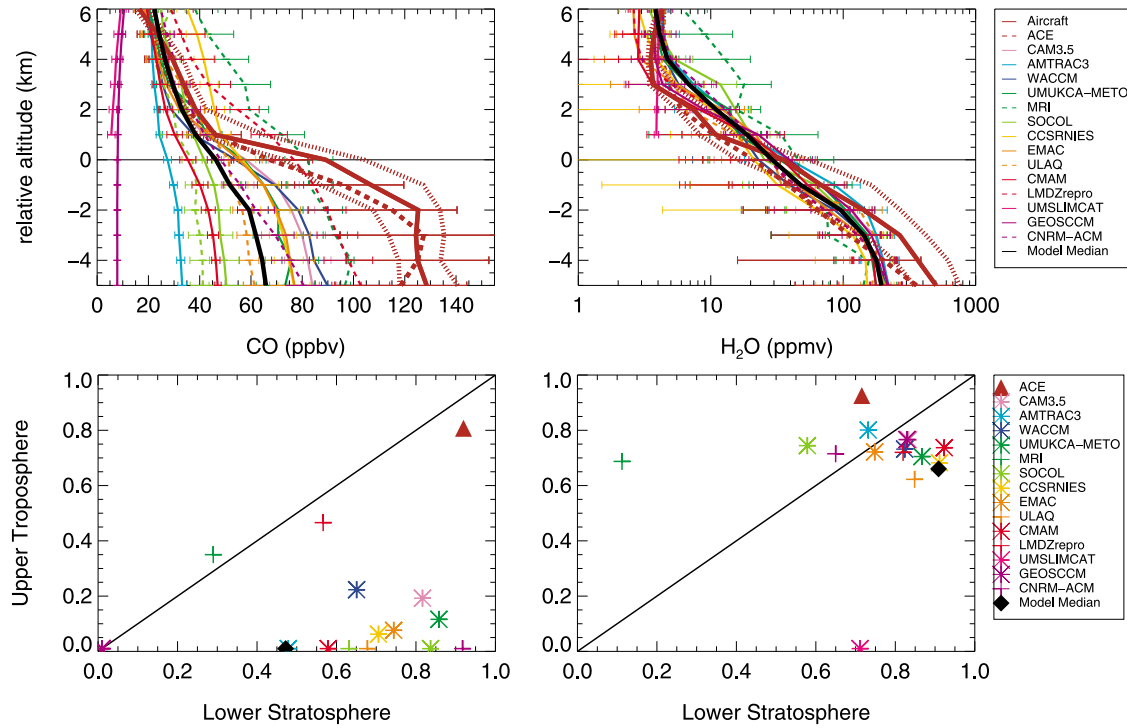


Figure 17. (left) CO and (right) H₂O vertical profiles (top) in tropopause coordinates and (bottom) corresponding grading for the UT and LS. Models and their 1σ -uncertainty (error bars) are given in color, and the multimodel mean is in black. Aircraft data are indicated with the brown solid line together with their 1σ -uncertainty (brown thin dashed line). Also indicated are ACE-FTS satellite data (brown thick dashed line and brown triangles).

due to overestimation of transport across the extratropical tropopause. In fact, the SOCOL-models score low in $W1$ in both seasons.

[69] In general models tend to transport too much of the tropospheric tracer into the LMS in winter as indicated by the low values of $W1$ in Table 3. However, most models capture the separation (i.e. the change of gradient) around $d\Theta = 30$ K indicated by $W2$. Thus most models are able to separate between transport across the local tropopause in the extratropics and processes involving other time scales and source regions. During summer, the models are capable of capturing the increase in tropospheric influence from the subtropics. The high summer values of $W2$ are a result of weaker differences in the vertical gradients in the two layers due to the enhanced transport from the subtropics accompanied with larger variability found in the measurements.

[70] The best overall representation of transport and coupling is seen in CAM3.5, CMAM, CNRM-ACM, EMAC, UMUKCA-METO and WACCM, whereas LMDZrepro and Niwa-SOCOL seem to be too diffusive or permeable across the tropopause, confirming the results of the previous diagnostic using seasonal cycles. Most models tend to get the separation between the different regimes in the LMS (UT, transition layer, background LMS) right within the measurements' variability.

4.2.4. Vertical Profiles in Tropopause Coordinates

[71] The vertical structure of H₂O and CO across the tropopause is evaluated using profiles in tropopause coordinates [Logan et al., 1999; Pan et al., 2004, 2007; Considine et al., 2008; Hegglin et al., 2006, 2009]. Tropopause coordinates

have been shown to effectively decrease tracer variability due to geophysical variability (i.e. day-to-day variations in tropopause height) in the region of ± 3 km and 5 km from the tropopause in summer/autumn and winter/spring, respectively [Hegglin et al., 2008]. The diagnostic requires instantaneous model output. For consistency with the coverage of the aircraft data [Tilmes et al., 2010], models are evaluated for the years between 1995 and 2005.

[72] The region of analysis is chosen to be the part of the extratropics that is not strongly influenced by the subtropical tropopause break and double tropopauses. Selection criteria were: a tropopause height of ≤ 325 K in winter and spring and ≤ 335 K in summer and fall, the absence of double tropopauses, and a latitude equatorward of 80°N . The profiles selected are largely within 40 – 80°N . The chemical composition of the lower stratosphere, as already discussed in the introduction, is largely controlled by the downward transport of aged stratospheric air via the Brewer-Dobson circulation, with seasonally varying contribution from isentropic mixing between tropical and high latitudes. The region is therefore well suited for evaluating how well models represent the two competing processes. The vertical structure is examined using H₂O and CO using annual mean distributions. The CO evaluation can be seen as an extension of the metric using normalized vertical profiles of CO (see Section 4.2.3). A mean value is derived from observations and models for both the UT (with data between 1 and 5 km below the tropopause) and LS (with data between 1 and 5 km above the tropopause) and used to calculate grades according to equation (8).

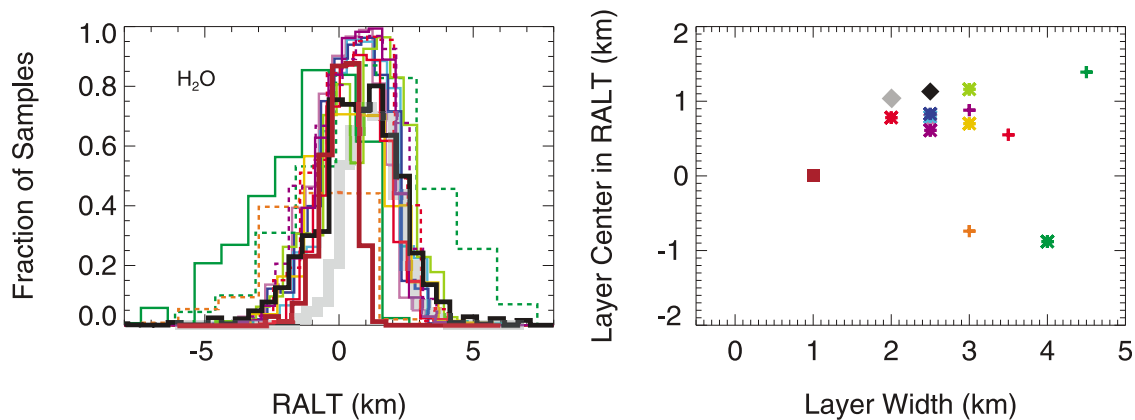


Figure 18. (left) Fraction of air parcels within the ExTL plotted as a function of the distance relative to the thermal tropopause (in arbitrary units, not normalized between models) for models from year 2000 (colors; see Figure 17 legend), for aircraft observations from 1997 and 40°N–80°N between spring and fall (brown solid line), and for ACE-FTS satellite data from 2004–2007 and 60°N–70°N (gray thick line). Black line indicates the multimodel mean. (right) Scatterplot between center and width of the ExTL. Brown square indicates aircraft observations, gray diamond denotes ACE-FTS data, colored symbols are the different models (see Figure 17 legend), and black diamond is the multimodel mean.

[73] The CO and H₂O vertical structures and the grading values are shown in Figure 17. Most models are not yet designed to simulate tropospheric chemistry and anthropogenic fuel or biomass burning sources of CO, resulting in a significant underestimation of the simulated CO in the UT compared to the observations (Figure 17, left), but good agreement is generally found for the LS. This can be seen in Figure 17 (bottom left) where grades are shown to be close to zero for the UT, but generally higher than 0.5 for the LS. However, even the models including tropospheric chemistry (CAM3.5, EMAC, and ULAQ) underestimate the CO vertical profiles substantially. H₂O is well simulated by the models in both the UT and LS, except for MRI which shows too high values in the LS. The corresponding grades (Figure 17, bottom right) are clustered at values of 0.7 for the UT and 0.8 for the LS. The differences between observations and models, although smaller than those observed in CO, may have significant implications for the simulation of surface climate [Forster and Shine, 1997; Solomon et al., 2010]. The comparison with the ACE-FTS satellite data indicates a good agreement between the two data sets, within their uncertainties. Differences between satellite and aircraft observations may be due to the coarser vertical resolution in the satellite data and/or the smaller regional coverage of aircraft observations. A final grade is calculated by averaging the UT and LS H₂O grades for each model and is listed in the summary matrix.

4.2.5. ExTL Depth From Tracer-Tracer Correlations

[74] The extratropical tropopause transition layer (ExTL) exhibits air masses with a mixed composition of partly tropospheric, partly stratospheric air [Fischer et al., 2000; Haynes and Shepherd, 2001; Hoor et al., 2002; Pan et al., 2004]. The representation of the ExTL characterizes how well the models reproduce the tropopause as a transport barrier and its sharpness. The transition layer depth and center location is examined using the tracer-tracer correlation method applied to O₃ and H₂O [Pan et al., 2007; Hegglin et al., 2009]. A stratospheric branch is identified using a fit

to a polynomial function of second order to all data points in the LS (<20 km) with H₂O < 10 ppmv. Similarly, a tropospheric branch is represented by a linear function derived by fitting all data points with O₃ < 100 ppbv for both observations and models. Mixed air masses are identified as those points outside the 3 σ range of both the stratospheric branch and the tropospheric branch. The fractional distribution of the identified air parcels is then plotted as a function of their distance from the thermal tropopause (in Figure 18). The observed transition layer is derived using POLARIS aircraft data in the NH, which include measurements in spring, summer and fall [Pan et al., 2007]. The model output was chosen for the same latitudes and from the same seasons. Note that the ExTL depth derived from the O₃–H₂O pair is different from the one obtained using the O₃–CO pair [Hegglin et al., 2009]. The different ExTL depths are explained by the fact that H₂O is strongly affected by the minimum temperature an air parcel experiences during its travel across the tropopause into the stratosphere, and its longer life-time compared to CO once it enters the stratosphere.

[75] Two parameters are used to quantify the comparisons: a) the center of the ExTL, defined as the center point of the distribution at the half maximum, and b) the ExTL width, defined as the width at half maximum of the probability density function. These criteria are influenced by the bin size, which was chosen as 0.5 km for the observations and for the models adjusted to their vertical resolution (0.5 or 1 km). ExTL width and center are shown in Figure 18 (right). The ExTL is well manifested in most models. However, in all cases the ExTL is broader, between 2 and 4 km, compared to 1 km derived from the observations. Further, the models' layer centers are shifted upward by about 1 km in most cases. Observations from the ACE-FTS satellite are also shown (observations taken from Figure 3 of Hegglin et al. [2009]). ACE-FTS has an effective resolution similar to the CCMs (around 1 km) and shows a behavior similar to that of AMTRAC3, CAM3.5, CMAM,

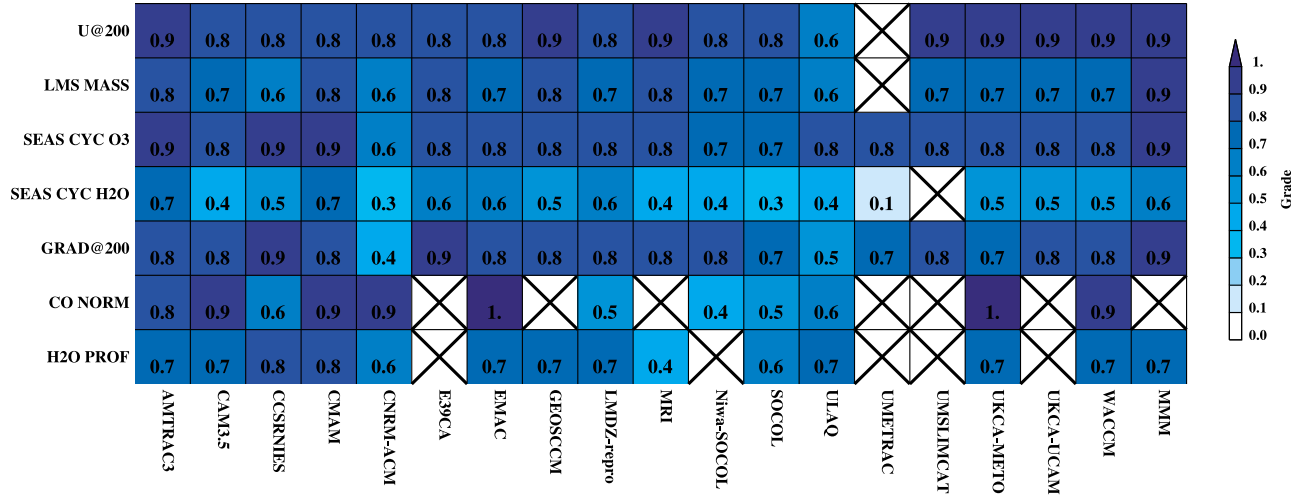


Figure 19. Summary of metrics used to quantitatively evaluate the different models. ‘MMM’ denotes the multimodel mean. The diagnostics used as metrics are: ‘U@200’ the zonal mean zonal wind at 200 hPa (Section 4.1.1), ‘SEAS CYC O3’ and ‘SEAS CYC H2O’ the seasonal cycle of the tracers (Section 4.2.1), ‘GRAD@200’ the meridional gradient in O₃ at 200 hPa (Section 4.2.2), ‘CO NORM’ the normalized vertical CO profiles in tropopause coordinates (Section 4.2.3), and ‘H2O PROF’ H₂O profiles in tropopause coordinates (Section 4.2.4). Numbers indicate the lower bound of the color-range. Models with grades larger than 0.6 are considered to perform satisfactorily.

GEOSCCM, and WACCM, exhibiting a layer width of 2 km and a layer center at 1 km above the thermal tropopause. The limited resolution of the models is therefore likely the primary cause for this shift. Indeed, a higher resolution model by Miyazaki *et al.* [2010a] is capable of better resolving the fine-scale structure of the ExTL. Uncertainties in tropopause locations derived from the relatively coarse vertical resolution of the models or lack of representativeness of the aircraft observations may also have contributed to the discrepancies.

5. Discussion of Model Performance

5.1. Quantitative Discussion

[76] The quantitative results of the metrics listed in Section 3.2 and discussed in more detail in the main body of this paper are compiled in the summary matrix (Figure 19). Note that the grading often involves subjective choices and is sensitive to observational errors. However, while the models often reach very high scores, indicating a good model performance in the extratropical UTLS, there are also some obvious deficiencies. The models score better in metrics testing dynamics (zonal mean zonal wind and LMS mass) rather than transport and mixing (seasonal cycle of O₃ and H₂O, meridional gradient in O₃, normalized and absolute vertical profiles), and better in metrics focusing on the LS (seasonal cycle of O₃ at 100 hPa, meridional gradient in O₃) rather than the transition between the troposphere and the stratosphere (seasonal cycle of O₃ and H₂O at 200 hPa, and normalized and absolute vertical profiles). This may be simply due to the length-scales of the chemical and dynamical structures which are much smaller in the tropopause region than in the stratosphere. At least for the distribution of O₃, the lack of tropospheric chemistry or

limitations in its representation may also contribute to the poorer performance of the models in the transition region. Note, however, that models including a more comprehensive tropospheric chemistry are not seen to perform better than the others. The multimodel mean generally scores higher than any individual model, except for the seasonal cycle of H₂O. In fact, most models seem to score lower in this latter metric, which is likely due to the uncertainty in the observations as discussed in Section 4.2.1. The fact that the multimodel mean scores so well on all diagnostics suggests that there are no significant missing processes in the models, although particular models may have significant deficiencies in their representation of the processes.

[77] Two models score consistently higher than 0.7 throughout the different extratropical UTLS metrics: AMTRAC3 and CMAM. CMAM may deserve a special note, since it has a relatively low horizontal resolution (T31), which would usually be expected to limit model performance. However, the ratio of vertical to horizontal resolution may be more important [Fox-Rabinovitz and Lindzen, 1993]. Also the spectral transport scheme is known not to be diffusive. Other models that perform well are CAM3.5, E39CA, EMAC, GEOSCCM, the UMOUKA-models, and WACCM with the only grade lower than 0.7 being the metric of the seasonal cycle of H₂O. Moderately performing models are CCSRNIES, LMDZ-repro, and MRI. The lowest scoring models are CNRM-ACM, the SOCOL-models, and ULAQ showing lower values than average for most of the extratropical UTLS metrics. The SOCOL-models may score low due to a combination of their hybrid transport scheme and a relatively low horizontal (T30) and vertical resolution (5 levels in the UTLS), and ULAQ due to its very low horizontal (11.5° × 22.5°) and vertical resolution (3 levels in the UTLS) and its quasi-geostrophic dynamical core. CNRM-ACM also uses a cubic semi-Lagrangian transport

scheme. UMETRAC and UMSLIMCAT are not rated here since they lack grades for more than two diagnostics.

5.2. Qualitative Discussion

5.2.1. Seasonal Zonal Mean Zonal Wind

[78] Most models perform well in reproducing this quantity, reflecting that the thermal structure and therefore the basic dynamical state of the atmosphere is well represented in the models. One exception to this is ULAQ. This might be due to an insufficient horizontal and/or vertical resolution and the quasi-geostrophic dynamical core which introduces errors in the thermal wind balance.

5.2.2. Seasonal Cycle of LMS Mass

[79] Most models represent well the phase and amplitude of the seasonal cycle of LMS mass, but not so the annual mean value in LMS mass. Overall scores are generally higher for the NH than for the SH. Models scoring high are AMTRAC3, CMAM, E39CA, and GEOSCCM. Models that perform poorly are CCSRNIES, CNRM-ACM, and ULAQ. The diagnostic yields insight into the strength and seasonality of the Brewer-Dobson circulation which will affect stratosphere-troposphere exchange and therefore both UT and LS tracer distributions.

5.2.3. Tropopause Pressure Anomalies

[80] Although the models seem to reproduce the seasonal cycle of tropopause pressure well in the NH (which is supported by the metric of LMS mass), they show more problems in representing interannual variability. CNRM-ACM has unrealistically large interannual variability and low tropopause pressure. CCSRNIES, EMAC, ULAQ and WACCM perform worst among the models, with both too high/low mean values and very small correlation with the structure of the observed variability.

5.2.4. Tropopause Inversion Layer

[81] Most models simulate a clear TIL with a strong maximum in N^2 just above the extratropical tropopause, except CCSRNIES which shows a more monotonic increase in N^2 across the tropopause. The models also simulate correctly the seasonal cycle of the TIL with stronger maxima in summer than during winter. However, the maximum in the TIL is shifted to slightly higher altitudes above the tropopause than expected from full-resolution observations. Degrading the resolution of the observations shows a closer match with the models and yields a more meaningful model-measurement comparison.

5.2.5. Seasonal Cycles in O_3 , HNO_3 , and H_2O at 100 and 200 hPa

[82] Most models perform reasonably well for O_3 in the NH, however the amplitude is consistently too high at 100 hPa and too low at 200 hPa. The latter finding indicates that the models exhibit too much transport from the tropics at and above 100 hPa, and across the tropopause at 200 hPa. The spread in skill in representing H_2O is larger than for O_3 , with models doing better at 100 hPa than at 200 hPa. At 200 hPa, strong tropospheric influence causes too large amplitudes in the seasonal cycle. Note that there exist large observational uncertainties in H_2O at the 200 hPa level. Better measurements are needed to gain more confidence in this quantitative metric. The spread in skill at representing HNO_3 in the SH at 200 hPa is even larger. UMSLIMCAT shows the highest score, but most other models have a low

correlation with observations and underestimate the annual cycle amplitude. The CCSRNIES and the SOCOL-models seem to perform worst.

5.2.6. Sharpness of Meridional Gradients in O_3

[83] The results of this metric are largely consistent with those from the seasonal cycle of O_3 at 200 hPa. Models generally are capable of maintaining a clear distinction between the tropical UT and the extratropical LS, as indicated in strong maxima in the gradient at the location of the subtropical jet. However, some models overestimate (UMSLIMCAT and UМУKCA-METO) and some underestimate (CNRM-ACM and ULAQ) the maximum value in the gradient.

5.2.7. Normalized CO in Potential Temperature Relative to the Tropopause Height

[84] Most models perform reasonably well in this diagnostic, except LMDZrepro, SOCOL, and Niwa-SOCOL, which have too much transport across the extratropical tropopause. The SOCOL-models have a semi-Lagrangian transport scheme which together with a relatively low vertical and horizontal resolution may contribute to the models being too diffusive.

5.2.8. Vertical Profiles of H_2O and CO in Tropopause Coordinates

[85] The models show some difficulties simulating the seasonal mean vertical profiles of the different tracers. Models perform better for H_2O , possibly because it is primarily affected by the tropopause temperature and less affected by chemistry and global-scale transport than CO. CO is represented poorly, primarily because most models do not include tropospheric chemistry or treat it in a simplified way. Note however that CAM3.5 which includes tropospheric chemistry shows about the same CO profile as WACCM which does not include tropospheric chemistry. EMAC and ULAQ also have a comprehensive tropospheric chemistry, however they do not perform remarkably better than the other models. The lack of a more sophisticated tropospheric chemistry will likely result in poor UT O_3 distributions, which remains to be tested in a future assessment.

5.2.9. Depth of the Extratropical Tropopause Transition Layer

[86] The models simulate an extratropical tropopause transition layer (ExTL) that is deeper than observed in aircraft observations, and shifted above the thermal tropopause. This is likely due to the models' limited vertical resolutions, as comparison with the ACE-FTS satellite observations indicates, which have a resolution more similar to that of the models. On the other hand, the aircraft measurements may lack representativeness. CMAM scores best in this metric, which is noteworthy since CMAM has a relatively low horizontal resolution compared to other models. The ratio between vertical and horizontal resolution might matter more. Models that show most difficulties in reproducing the ExTL are SOCOL, UМУKCA-METO, and CNRM-ACM, whose transport schemes may be too diffusive. Also rather poor performance is seen for CCSRNIES, LMDZrepro, and MRI.

6. Conclusions

[87] We have presented here the first multimodel assessment of chemistry-climate models (CCMs) in the extratropical

upper troposphere/lower stratosphere (UTLS) – a region of the atmosphere important to different aspects of chemistry–climate coupling. Different diagnostics have been used to characterize model performance and the results are discussed in more detail in Sections 5.1 and 5.2. A main finding of our evaluations is that the CCMs represent the main dynamical and chemical characteristics relatively well despite their limited horizontal and vertical resolution.

[88] Why do the CCMs perform relatively well in the UTLS despite resolution issues? The models get the basic wave-driven dynamics right of (a) the stratospheric Brewer–Dobson circulation, and (b) the tropospheric baroclinic general circulation in the extratropics. The basic (stratospheric) chemistry for ozone and condensation of water vapor is also captured. These abilities allow the models to capture the basic dynamical climatology, and with appropriate transport schemes, can properly approximate transport and thereby tracer distributions on a climatological basis. For the tropopause inversion layer (TIL), it is the large scale dynamics, a good representation of the distributions of radiatively-active tracers, and a proper representation of radiative transfer, that allow the models to represent a stability inversion above the tropopause. However, as discussed above, the low vertical resolution in CCMs biases the TIL with respect to high resolution observations. The ExTL is a product of the large scale dynamics and resulting transport with basic tracer chemistry, and in the UTLS the combination of large scale diabatic transport, quasi-isentropic transport and mixing with the tropics across seasonally variable subtropical transport barriers, and cross-isentropic transport and mixing at the extratropical tropopause. In the models these features are represented with sufficient fidelity to reproduce tracer gradients in the ExTL.

[89] For a better representation of the UTLS in the future, CCMs will need to improve in a few key areas. Increased vertical resolution will help represent the fine-scale structures of the TIL and ExTL. Tropospheric chemistry and increased horizontal resolution are also important for improving model representation of gradients across the tropopause. As part of this development, CCMs should add a range of very short-lived species (VSLs) that represent major reservoirs of source gases for stratospheric bromine. VSLs can be used as process-specific transport diagnostics. These tracers provide a range of life times and can discriminate transport from marine and continental source regions into the UTLS.

[90] Our results further demonstrate that the UTLS is still relatively sparsely sampled by observations which unfortunately limits confidence in the quantitative evaluation of model performance in the UTLS (see Figures 11 and 12 and related discussion). It will be necessary to compare the metrics applied here with future measurements to reduce uncertainty in the model comparison associated with potential measurement errors. The observational data-base for the UTLS needs to be expanded by measurements with both higher spatial and temporal resolution and sampling, but also reasonable accuracy. New observations are needed especially for O₃ and H₂O in the UTLS with a vertical resolution better than 1 km and a horizontal resolution better than 100 km, especially in the SH, the tropics, and the upper troposphere.

[91] **Acknowledgments.** Thanks go to Diane Pendlebury and Mike Neish (University of Toronto) for technical assistance with figures and the CCMVal-2 data. M.I. Hegglin has been supported by the Canadian Foundation for Climate and Atmospheric Sciences (CFCAS) and the Canadian Space Agency (CSA) through the C-SPARC network, which supports CMAM. Research at the Jet Propulsion Laboratory, California Institute of Technology was done under contract with the National Aeronautics and Space Administration. CCSRNIES research was supported by a grant-in-aid for scientific research from Ministry of Education, Culture, Sports, Science, and Technology (MEXT) of Japan (19340138) and the Global Environmental Research Fund of the Ministry of the Environment of Japan (A-071 and A-0903). Both CCSRNIES and MRI simulations were completed with the supercomputer at the National Institute for Environmental Studies (NIES), Japan. The contribution of the Met Office Hadley Centre was supported by the Joint DECC and Defra Integrated Climate Programme, DECC/Defra (GA01101). European contributions were supported by the European Commission through the SCOUT-O3 project under the 6th Framework Programme. WACCM-hires simulations were performed at the Centro de Supercomputación de Galicia. We acknowledge the Chemistry–Climate Model Validation (CCMVal) Activity of WCRP's (World Climate Research Programme) SPARC (Stratospheric Processes and their Role in Climate) project for organizing and coordinating the model data analysis activity, and the British Atmospheric Data Centre (BADC) for collecting and archiving the CCMVal model output.

References

- Akiyoshi, H., L. B. Zhou, Y. Yamashita, K. Sakamoto, M. Yoshiki, T. Nagashima, M. Takahashi, J. Kurokawa, M. Takigawa, and T. Imamura (2009), A CCM simulation of the breakup of the Antarctic polar vortex in the years 1980–2004 under the CCMVal scenarios, *J. Geophys. Res.*, **114**, D03103, doi:10.1029/2007JD009261.
- Anthes, R. A., et al. (2008), The COSMIC/FORMOSAT-3 mission: Early results, *Bull. Am. Meteorol. Soc.*, **89**, 313–333.
- Appenzeller, C., J. R. Holton, and K. H. Rosenlof (1996), Seasonal variation of mass transport across the tropopause, *J. Geophys. Res.*, **101**, 15,071–15,078.
- Austin, J., and N. Butchart (2003), Coupled chemistry–climate model simulation for the period 1980 to 2020: Ozone depletion and the start of ozone recovery, *Q. J. R. Meteorol. Soc.*, **129**, 3225–3249.
- Austin, J., and R. J. Wilson (2010), Sensitivity of polar ozone to sea surface temperatures and halogen amounts, *J. Geophys. Res.*, **115**, D18303, doi:10.1029/2009JD013292.
- Baldwin, M. P., and T. J. Dunkerton (2001), Stratospheric harbingers of anomalous weather regimes, *Science*, **244**, 581–584.
- Bell, S. W., and M. Geller (2008), Latitudinal variations in Birner's extratropical transition layer, *J. Geophys. Res.*, **113**, D05109, doi:10.1029/2007JD009022.
- Bernath, P. F., et al. (2005), Atmospheric Chemistry Experiment (ACE): Mission overview, *Geophys. Res. Lett.*, **32**, L15S01, doi:10.1029/2005GL022386.
- Berthet, G., J. G. Esler, and P. H. Haynes (2007), A Lagrangian perspective of the tropopause and the ventilation of the lowermost stratosphere, *J. Geophys. Res.*, **112**, D18102, doi:10.1029/2006JD008295.
- Birner, T. (2006), Fine-scale structure of the extratropical tropopause region, *J. Geophys. Res.*, **111**, D04104, doi:10.1029/2005JD006301.
- Birner, T., A. Dörnbrack, and U. Schumann (2002), How sharp is the tropopause at midlatitudes?, *Geophys. Res. Lett.*, **29**(14), 1700, doi:10.1029/2002GL015142.
- Bönisch, H., A. Engel, J. Curtius, T. Birner, and P. Hoor (2009), Quantifying transport into the lowermost stratosphere using simultaneous in-situ measurements of SF₆ and CO₂, *Atmos. Chem. Phys.*, **9**, 5905–5919.
- Boone, C. D., et al. (2005), Retrievals for the Atmospheric Chemistry Experiment Fourier Transform Spectrometer, *Appl. Opt.*, **44**, 7218–7231.
- Bregman, A., J. Lelieveld, M. van den Broek, P. Siegmund, H. Fischer, and O. Bujok (2000), N₂O and O₃ relationship in the lowermost stratosphere: A diagnostic for mixing processes as represented by a three-dimensional chemistry–transport model, *J. Geophys. Res.*, **105**, 17,279–17,290, doi:10.1029/2000JD900035.
- Brunner, D., et al. (2003), An evaluation of the performance of chemistry transport models by comparison with scientific aircraft observations. Part 1: Concepts and overall model 2076 performance, *Atmos. Chem. Phys.*, **3**, 1609–1631.
- Brunner, D., et al. (2005), An evaluation of the performance of chemistry transport models. Part 2: Detailed comparison with two selected campaigns, *Atmos. Chem. Phys.*, **5**, 107–129.
- Clerbaux, C., et al. (2008), CO measurements from the ACE-FTS satellite instrument: Data analysis and validation using ground-based, airborne and spaceborne observations, *Atmos. Chem. Phys.*, **8**, 2569–2594.

- Clough, S., and M. Iacono (1995), Line-by-line calculation of atmospheric fluxes and cooling rates: 2. Application to carbon dioxide, ozone, methane, nitrous oxide and the halocarbons, *J. Geophys. Res.*, **100**, 16,519–16,535, doi:10.1029/95JD01386.
- Considine, D. B., J. A. Logan, and M. A. Olsen (2008), Evaluation of near-tropopause ozone distributions in the Global Modeling Initiative combined stratosphere/troposphere model with ozonesonde data, *Atmos. Chem. Phys.*, **8**, 2365–2385.
- de Grandpré, J., S. R. Beagley, V. I. Fomichev, E. Griffioen, J. C. McConnell, A. S. Medvedev, and T. G. Shepherd (2000), Ozone climatology using interactive chemistry: Results from the Canadian Middle Atmosphere Model, *J. Geophys. Res.*, **105**, 26,475–26,491.
- Déqué, M. (2007), Frequency of precipitation and temperature extremes over France in an anthropogenic scenario: Model results and statistical correction according to observed values, *Global Planet. Change*, **57**, 16–26.
- Douglass, A. R., M. J. Prather, T. M. Hall, S. E. Strahan, P. J. Rasch, L. C. Sparling, L. Coy, and J. M. Rodriguez (1999), Choosing meteorological input for the global modeling initiative assessment of high-speed aircraft, *J. Geophys. Res.*, **104**, 27,545–27,564.
- Dupuy, E., et al. (2009), Validation of ozone measurements from the Atmospheric Chemistry Experiment (ACE), *Atmos. Chem. Phys.*, **9**, 287–343.
- Egorova, T., E. Rozanov, V. Zubov, E. Manzini, W. Schmutz, and T. Peter (2005), Chemistry climate model SOCOL: A validation of the present-day climatology, *Atmos. Chem. Phys.*, **5**, 1557–1576.
- Engel, A., et al. (2006), Highly resolved observations of trace gases in the lowermost stratosphere and upper troposphere from the SPURT project: An overview, *Atmos. Chem. Phys.*, **6**, 283–301.
- Eyring, V., et al. (2006), Assessment of temperature, trace species and ozone in chemistry-climate model simulations of the recent past, *J. Geophys. Res.*, **111**, D22308, doi:10.1029/2006JD007327.
- Eyring, V., et al. (2007), Multimodel projections of stratospheric ozone in the 21st century, *J. Geophys. Res.*, **112**, D16303, doi:10.1029/2006JD008332.
- Eyring, V., M. P. Chipperfield, M. A. Giorgetta, D. E. Kinnison, E. Manzini, K. Matthes, P. A. Newman, S. Pawson, T. G. Shepherd, and D. W. Waugh (2008), Overview of the New CCMVal reference and sensitivity simulations in support of upcoming ozone and climate assessments and the planned SPARC CCMVal report, *SPARC Newsl.*, **30**, 20–26.
- Fischer, H., F. G. Wienhold, P. Hoor, O. Bujok, C. Schiller, P. Siegmund, M. Ambaum, H. A. Scheeren, and J. Lelieveld (2000), Tracer correlations in the northern high latitude lowermost stratosphere: Influence of cross-tropopause mass exchange, *Geophys. Res. Lett.*, **27**(1), 97–100, doi:10.1029/1999GL010879.
- Fischer, H., et al. (2008), MIPAS: An instrument for atmospheric and climate research, *Atmos. Chem. Phys.*, **8**, 2151–2188.
- Flocke, F., et al. (1999), An examination of chemistry and transport processes in the tropical lower stratosphere using observations of long-lived and short-lived compounds obtained during STRAT and POLARIS, *J. Geophys. Res.*, **104**, 26,625–26,642.
- Forster, P., and K. Shine (1997), Radiative forcing and temperature trends from stratospheric ozone changes, *J. Geophys. Res.*, **102**, 10,841–10,855, doi:10.1029/96JD03510.
- Fox-Rabinovitz, M., and R. S. Lindzen (1993), Numerical experiments on consistent horizontal and vertical resolution for atmospheric models and observing systems, *Mon. Weather Rev.*, **121**, 264–271.
- Garcia, R. R., D. R. Marsh, D. E. Kinnison, B. A. Boville, and F. Sassi (2007), Simulation of secular trends in the middle atmosphere, 1950–2003, *J. Geophys. Res.*, **112**, D09301, doi:10.1029/2006JD007485.
- Garny, H., M. Dameris, and A. Stenke (2009), Impact of prescribed SSTs on climatologies and long-term trends in CCM simulations, *Atmos. Chem. Phys.*, **9**, 6017–6031.
- Gettelman, A., et al. (2009), The tropical tropopause layer 1960–2100, *Atmos. Chem. Phys.*, **9**, 1621–1637.
- Gettelman, A., et al. (2010), Multimodel assessment in the upper troposphere and lower stratosphere: Tropics and global trends, *J. Geophys. Res.*, **115**, D00M08, doi:10.1029/2009JD013638.
- Grewe, V., and R. Sausen (2009), Comment on “Quantitative performance metrics for stratospheric-resolving chemistry-climate models” by Waugh and Eyring, *Atmos. Chem. Phys.*, **9**, 9101–9110, doi:10.5194/acp-9-9109-2009.
- Grise, K. M., D. W. J. Thompson, and T. Birner (2010), A global survey of static stability, *J. Clim.*, **23**, 2275–2292.
- Haynes, P., and T. G. Shepherd (2001), Report on the SPARC tropopause workshop, *SPARC Newsl.*, **17**, 3–10.
- Hegglin, M. I., and T. G. Shepherd (2007), O₃-N₂O correlations from the Atmospheric Chemistry Experiment: Revisiting a diagnostic of transport and chemistry in the stratosphere, *J. Geophys. Res.*, **112**, D19301, doi:10.1029/2006JD008281.
- Hegglin, M. I., and T. G. Shepherd (2009), Large climate-induced changes in UV index and stratosphere-to-troposphere ozone flux, *Nat. Geosci.*, **2**, 687–691.
- Hegglin, M. I., et al. (2006), Measurements of NO, NO_y, N₂O, and O₃ during SPURT: Implications for transport and chemistry in the lowermost stratosphere, *Atmos. Chem. Phys.*, **6**, 1331–1350.
- Hegglin, M. I., C. D. Boone, G. L. Manney, T. G. Shepherd, K. A. Walker, P. F. Bernath, W. H. Daffer, P. Hoor, and C. Schiller (2008), Validation of ACE-FTS satellite data in the upper troposphere/lower stratosphere (UTLS) using non-coincident measurements, *Atmos. Chem. Phys.*, **8**, 1483–1499.
- Hegglin, M. I., C. D. Boone, G. L. Manney, and K. A. Walker (2009), A global view of the extratropical tropopause transition layer from Atmospheric Chemistry Experiment Fourier Transform Spectrometer O₃, H₂O, and CO, *J. Geophys. Res.*, **114**, D00B11, doi:10.1029/2008JD009984.
- Hints, E. J., E. M. Weinstock, J. G. Anderson, R. D. May, and D. F. Hurst (1999), On the accuracy of in situ water vapor measurements in the troposphere and lower stratosphere with the Harvard Lyman- α hygrometer, *J. Geophys. Res.*, **104**, 8183–8189.
- Holton, J. R., P. H. Haynes, M. E. McIntyre, A. R. Douglass, R. B. Rood, and L. Pfister (1995), Stratosphere-troposphere exchange, *Rev. Geophys.*, **33**(4), 403–439, doi:10.1029/95RG02097.
- Hoor, P., H. Fischer, L. Lange, J. Lelieveld, and D. Brunner (2002), Seasonal variations of a mixing layer in the lowermost stratosphere as identified by the CO-O₃ correlation from in situ measurements, *J. Geophys. Res.*, **107**(D5), 4044, doi:10.1029/2000JD000289.
- Hoor, P., C. Gurk, D. Brunner, M. I. Hegglin, H. Wernli, and H. Fischer (2004), Seasonality and extent of extratropical TST derived from in-situ CO measurements during SPURT, *Atmos. Chem. Phys.*, **4**, 1427–1442.
- Hoor, P., H. Fischer, and J. Lelieveld (2005), Tropical and extratropical tropospheric air in the lowermost stratosphere over Europe: A CO-based budget, *Geophys. Res. Lett.*, **32**, L07802, doi:10.1029/2004GL020218.
- Hoskins, B. J. (1991), Towards a PV- θ view of the general circulation, *Tellus, Ser. A*, **43**, 27–35.
- Intergovernmental Panel on Climate Change (2001), *Climate Change 2001: The Scientific Basis. Contribution of Working Group I to the Third Assessment Report of the Intergovernmental Panel on Climate Change*, edited by J. T. Houghton et al., Cambridge Univ. Press, Cambridge, U. K.
- Jöckel, P., et al. (2006), The atmospheric chemistry general circulation model ECHAM/MESSy1: Consistent simulation of ozone from the surface to the mesosphere, *Atmos. Chem. Phys.*, **6**, 5067–5104.
- Jourdain, L., S. Bekki, F. Lott, and F. Lefèvre (2008), The coupled chemistry model LMDz Reprobus: Description of a transient simulation of the period 1980–1999, *Ann. Geophys.*, **6**, 1391–1413.
- Kalnay, E., et al. (1996), The NCEP/NCAR 40-year reanalysis project, *Bull. Am. Meteorol. Soc.*, **77**, 437–471.
- Lamarque, J. F., D. E. Kinnison, P. G. Hess, and F. M. Vitt (2008), Simulated lower stratospheric trends between 1970 and 2005: Identifying the role of climate and composition changes, *J. Geophys. Res.*, **113**, D12301, doi:10.1029/2007JD009277.
- Livesey, N. J., et al. (2007), MLS Version 2.2 Level 2 data quality and description document, *Tech. Rep. JPL D-33509*, Jet Propul. Lab., Pasadena, Calif. (Available at <http://mls.jpl.nasa.gov>)
- Livesey, N. J., et al. (2008), Validation of Aura Microwave Limb Sounder O₃ and CO observations in the upper troposphere and lower stratosphere, *J. Geophys. Res.*, **113**, D15S02, doi:10.1029/2007JD008805.
- Logan, J. A., et al. (1999), Trends in the vertical distribution of ozone: A comparison of two analyses of ozonesonde data, *J. Geophys. Res.*, **104**, 26,373–26,399.
- Milz, M., et al. (2005), Water vapor distributions measured with the Michelson Interferometer for Passive Atmospheric Sounding on board Envisat (MIPAS/Envisat), *J. Geophys. Res.*, **110**, D24307, doi:10.1029/2005JD005973.
- Milz, M., et al. (2009), Validation of water vapor profiles (version 13) retrieved by the IMK/IAA scientific retrieval processor based on full resolution spectra measured by MIPAS on board Envisat, *Atmos. Meas. Tech.*, **2**, 379–399.
- Miyazaki, K., K. Sato, S. Watanabe, Y. Tomikawa, Y. Kawatani, and M. Takahashi (2010a), Transport and mixing in the extratropical tropopause region in a high vertical resolution GCM. Part I: Potential vorticity and heat budget analysis, *J. Atmos. Sci.*, **67**, 1293–1314.
- Miyazaki, K., S. Watanabe, Y. Kawatani, Y. Tomikawa, M. Takahashi, and K. Sato (2010b), Transport and mixing in the extratropical tropopause region in a high vertical resolution GCM. Part II: Relative importance of large-scale and small-scale dynamics, *J. Atmos. Sci.*, **67**, 1315–1336.
- Morgenstern, O., et al. (2009), Evaluation of the new UKCA climate-composition model. Part I: The stratosphere, *Geosci. Model Dev.*, **1**, 43–57.

- Morgenstern, O., et al. (2010), Review of present-generation stratospheric chemistry-climate models and associated external forcings, *J. Geophys. Res.*, **115**, D00M02, doi:10.1029/2009JD013728.
- Newman, P. A., D. W. Fahey, W. H. Brune, and M. J. Kurylo (1999), Preface to special section: Photochemistry of Ozone Loss in the Arctic Region in Summer (POLARIS), *J. Geophys. Res.*, **104**, 26,481–26,495.
- Pan, L. L., W. J. Randel, B. L. Gary, M. J. Mahoney, and E. J. Hintsa (2004), Definitions and sharpness of the extratropical tropopause: A trace gas perspective, *J. Geophys. Res.*, **109**, D23103, doi:10.1029/2004JD004982.
- Pan, L. L., J. C. Wei, D. E. Kinnison, R. R. Garcia, D. J. Wuebbles, and G. P. Brasseur (2007), A set of diagnostics for evaluating chemistry-climate models in the extratropical tropopause region, *J. Geophys. Res.*, **112**, D09316, doi:10.1029/2006JD007792.
- Pawson, S., R. S. Stolarski, A. R. Douglass, P. A. Newman, J. E. Nielsen, S. M. Frith, and M. L. Gupta (2008), Goddard Earth Observing System chemistry-climate model simulations of stratospheric ozone-temperature coupling between 1950 and 2005, *J. Geophys. Res.*, **113**, D12103, doi:10.1029/2007JD009511.
- Pitari, G., E. Mancini, V. Rizzi, and D. Shindell (2002), Impact of future climate and emission changes on stratospheric aerosols and ozone, *J. Atmos. Sci.*, **59**, 414–440.
- Randel, W. J., and I. M. Held (1991), Phase speed spectra of transient eddy fluxes and critical layer absorption, *J. Atmos. Sci.*, **48**, 688–697.
- Randel, W. J., et al. (2003), The SPARC intercomparison of middle-atmosphere climatologies, *J. Clim.*, **17**, 986–1003.
- Randel, W. J., F. Wu, and P. Forster (2007), The extratropical tropopause inversion layer: Global observations with GPS data, and a radiative forcing mechanism, *J. Atmos. Sci.*, **64**, 4489–4496.
- Rosenlof, K., A. F. Tuck, K. K. Kelly, J. M. Russell, and M. P. McCormick (1997), Hemispheric asymmetries in water vapor and inferences about transport in the lower stratosphere, *J. Geophys. Res.*, **102**, 13,213–13,234.
- Schoeberl, M. R. (2004), Extratropical stratosphere-troposphere mass exchange, *J. Geophys. Res.*, **109**, D13303, doi:10.1029/2004JD004525.
- Schraner, M., et al. (2008), Technical note: Chemistry-climate model SOCOL: Version 2.0 with improved transport and chemistry/microphysics schemes, *Atmos. Chem. Phys.*, **8**, 5957–5974.
- Scinocca, J. F., N. A. McFarlane, M. Lazare, J. Li, and D. Plummer (2008), Technical note: The CCCma third generation AGCM and its extension into the middle atmosphere, *Atmos. Chem. Phys.*, **8**, 7055–7074.
- Shepherd, T. G. (2002), Issues in stratosphere-troposphere coupling, *J. Meteorol. Soc. Jpn.*, **80**, 769–792.
- Shepherd, T. G. (2007), Transport in the middle atmosphere, *J. Meteorol. Soc. Jpn.*, **85B**, 165–191.
- Shibata, K., and M. Deushi (2008a), Long-term variations and trends in the simulation of the middle atmosphere 1980–2004 by the chemistry-climate model of the Meteorological Research Institute, *Ann. Geophys.*, **26**, 1299–1326.
- Shibata, K., and M. Deushi (2008b), Simulation of the stratospheric circulation and ozone during the recent past (1980–2004) with the MRI chemistry-climate model, *Tech. Rep. CGER Supercomput. Monogr. Rep. 13*, Natl. Inst. for Environ. Stud., Tsukuba, Japan.
- Solomon, S., K. H. Rosenlof, R. W. Portmann, J. S. Daniel, S. M. Davis, T. J. Sanford, and G.-K. Plattner (2010), Contributions of stratospheric water vapor to decadal changes in the rate of global warming, *Science*, **327**(5970), 1219–1223, doi:10.1126/science.1182488.
- SPARC (2002), SPARC Intercomparison of Middle Atmosphere Climatologies, *WMO/TD-1142*, 96 pp., World Meteorol. Org., Paris.
- Steck, T., et al. (2007), Bias determination and precision validation of ozone profiles from MIPAS-Envisat retrieved with the IMK-IAA processor, *Atmos. Chem. Phys.*, **7**, 3639–3662.
- Stenke, A., M. Dameris, V. Grewe, and H. Garmy (2009), Implications of Lagrangian transport for simulations with a coupled chemistry-climate model, *Atmos. Chem. Phys.*, **9**, 5489–5504.
- Taylor, K. E. (2001), Summarizing multiple aspects of model performance in a single diagram, *J. Geophys. Res.*, **106**, 7183–7192, doi:10.1029/2000JD900719.
- Teyss  dre, H., et al. (2007), A new tropospheric and stratospheric chemistry and transport model MOCAGE-climat for multi-year studies: Evaluation of the present-day climatology and sensitivity to surface processes, *Atmos. Chem. Phys.*, **7**, 5815–5860.
- Thompson, D. W. J., and J. M. Wallace (1998), The Arctic Oscillation signature in the wintertime geopotential height and temperature fields, *Geophys. Res. Lett.*, **25**, 1297–1300.
- Thompson, D. W. J., J. C. Furtado, and T. G. Shepherd (2006), On the tropospheric response to anomalous stratospheric wave drag and radiative heating, *J. Atmos. Sci.*, **63**, 2616–2629.
- Tian, W., and M. P. Chipperfield (2005), A new coupled chemistry-climate model for the stratosphere: The importance of coupling for future O₃-climate predictions, *Q. J. R. Meteorol. Soc.*, **131**, 281–304.
- Tian, W., M. P. Chipperfield, L. J. Gray, and J. M. Zawodny (2006), Quasi-biennial oscillation and tracer distributions in a coupled chemistry-climate model, *J. Geophys. Res.*, **111**, D20301, doi:10.1029/2005JD006871.
- Tilmes, S., et al. (2010), An aircraft based upper troposphere lower stratosphere O₃, CO, and H₂O climatology for the Northern Hemisphere, *J. Geophys. Res.*, **115**, D14303, doi:10.1029/2009JD012731.
- Uppala, S. M., et al. (2005), The ERA-40 re-analysis, *Q. J. R. Meteorol. Soc.*, **131**, 2961–3012, doi:10.1256/qj.04.176.
- von Clarmann, T., et al. (2003), Retrieval of temperature and tangent altitude pointing from limb emission spectra recorded from space by the Michelson Interferometer for Passive Atmospheric Sounding (MIPAS), *J. Geophys. Res.*, **108**(D23), 4736, doi:10.1029/2003JD003602.
- von Clarmann, T., et al. (2009), Retrieval of temperature, H₂O, O₃, HNO₃, CH₄, N₂O, ClONO₂ and ClO from MIPAS reduced resolution nominal mode limb emission measurements, *Atmos. Meas. Tech.*, **2**, 159–175.
- Wang, D. Y., et al. (2007), Validation of nitric acid retrieved by the IMK-IAA processor from MIPAS/ENVISAT measurements, *Atmos. Chem. Phys.*, **7**, 721–738.
- Waters, J. W., et al. (2006), The Earth Observing System Microwave Limb Sounder (EOS MLS) on the Aura satellite, *IEEE Trans. Geosci. Remote Sens.*, **44**, 1075–1092.
- Waugh, D. W., and V. Eyring (2008), Quantitative performance metrics for stratospheric-resolving chemistry-climate models, *Atmos. Chem. Phys.*, **8**, 5699–5713.
- World Meteorological Organization (1957), Meteorology—A three-dimensional science, *WMO Bull.*, **6**, 134–138.
- Zahn, A., et al. (2000), Identification of extratropical two-way troposphere-stratosphere mixing based on CARIBIC measurements of O₃, CO, and ultrafine particles, *J. Geophys. Res.*, **105**, 1527–1535.
- H. Akiyoshi, T. Nakamura, and Y. Yamashita, National Institute for Environmental Studies, Tsukuba, Ibaraki 305-8506, Japan.
- J. A. A  l, Environmental Physics Laboratory, Universidade de Vigo, E-32004 Ourense, Spain.
- J. Austin, Geophysical Fluid Dynamics Laboratory, NOAA, Princeton, NJ 08540, USA.
- A. Baumgaertner, C. Br  hl, P. Hoor, and P. J  ckel, Max Planck Institut f  r Chemie, D-55020 Mainz, Germany.
- S. Bekki, LATMOS, Institut Pierre-Simone Laplace, UVSQ, UMPC, CNRS/INSU, F-75252 Paris, France.
- P. Braesicke and J. A. Pyle, Department of Chemistry, University of Cambridge, Cambridge CB2 1TN, UK.
- N. Butchart and S. C. Hardiman, Met Office, Exeter EX1 3PB, UK.
- M. Chipperfield, S. Dhomse, and W. Tian, School of Earth and Environment, University of Leeds, Leeds LS2 9JT, UK.
- V. Eyring, M. Dameris, and H. Garmy, Deutsches Zentrum f  r Luft- und Raumfahrt, Institut f  r Physik der Atmosph  re, Oberpfaffenhofen, D-82234 We  sling, Germany.
- S. Frith and S. Pawson, Global Modelling and Assimilation Office, NASA Goddard Space Flight Center, Greenbelt, MD 20771, USA.
- A. Gettelman, D. E. Kinnison, J. F. Lamarque, L. L. Pan, and S. Tilmes, Atmospheric Chemistry Division, National Center for Atmospheric Research, 1850 Table Mesa Dr., Boulder, CO 80305, USA.
- M. I. Hegglin, R. Krichevsky, T. G. Shepherd, and K. A. Walker, Department of Physics, University of Toronto, 60 St. George Street, Toronto, ON M5S 1A7, Canada. (michaela@atmosph.physics.utoronto.ca)
- E. Mancini and G. Pitari, Dipartimento di Fisica, Universita degli Studi de L'Aquila, I-67010 Coppito (AQ), Italy.
- G. L. Manney, Jet Propulsion Laboratory, California Institute of Technology, Pasadena, CA 91109, USA.
- M. Michou, D. Oliv  , and H. Teyss  dre, GAME/CNRM, M  t  o-France, CNRS, F-31400 Toulouse, France.
- O. Morgenstern and D. Smale, National Institute of Water and Atmospheric Research, Lauder, New Zealand.
- D. A. Plummer, Environment Canada, Toronto, ON M3H 5T4, Canada.
- E. Rozanov, Physikalisches-Meteorologisches Observatorium Davos, CH-7260 Davos, Switzerland.
- J. F. Scinocca, Canadian Centre for Climate Modelling and Analysis, Victoria, BC V8P 5C2, Canada.
- K. Shibata, Meteorological Research Institute, Tsukuba, Ibaraki 305-0052, Japan.
- S.-W. Son, Department of Atmospheric and Oceanic Sciences, McGill University, Montreal, QC H3A 2T5, Canada.
- G. Stiller, Karlsruhe Institute of Technology, Institute for Meteorology and Climate Research, PO Box 3640, D-76021 Karlsruhe, Germany.
- D. Waugh, Department of Earth and Planetary Sciences, Johns Hopkins University, 3400 N. Charles St., Baltimore, MD 21218, USA.